Monthly Notices
of the
ROYAL ASTRONOMICAL SOCIETY

MNRAS **513,** 4899–4912 (2022)
Advance Access publication 2022 May 5

https://doi.org/10.1093/mnras/stac1211

Polarization, polarizing efficiency, and grain alignment towards the direction of the cluster NGC 2345

Sadhana Singh,[1,2]★ Jeewan C. Pandey [1]★ and Thiem Hoang[3,4]★

[1]*Aryabhatta Research Institute of Observational Sciences (ARIES), Manora Peak, Nainital 263001, India*
[2]*School of Studies in Physics & Astrophysics, Pt. Ravishankar Shukla University, Raipur 492010, India*
[3]*Korea Astronomy and Space Science Institute, Daejeon 34055, Republic of Korea*
[4]*Korea University of Science and Technology, 217 Gajeong-ro, Yuseong-gu, Daejeon 34113, Republic of Korea*

Accepted 2022 April 26. Received 2022 April 26; in original form 2021 October 22

ABSTRACT

We have investigated the grain alignment and dust properties towards the direction of the cluster NGC 2345 using the multiband optical polarimetric observations. For the majority of the stars, the observed polarization is found to be due to the interstellar medium with average values of maximum polarization and wavelength corresponding to it as 1.55 per cent and 0.58 μm, respectively. This reveals a similar size distribution of dust grains to that in the general interstellar medium in the direction of NGC 2345. Alteration of dust properties near the distance of 1.2 kpc towards the direction of NGC 2345 has been noticed. The dust grains located beyond this distance are found to be aligned with the Galactic magnetic field, whereas a dispersion in the orientation of the dust grains lying in the foreground of this distance is found. Polarizing efficiency of grains in this direction is found to be close to the average efficiency for our Galaxy. The decreased grain size along with the increased polarizing efficiency towards the core region of the cluster indicates the local radiation field is higher within the cluster, which is responsible for the increased alignment efficiency of small grains. The wavelength of maximum polarization (associated with the average size of aligned grains) is also found to increase with extinction and reduces with the increase in polarizing efficiency, which can be explained by the radiative torque alignment mechanism.

Key words: polarization – techniques: polarimetric – dust, extinction – open clusters and associations: individual: NGC 2345.

1 INTRODUCTION

The starlight passing through the interstellar medium (ISM) becomes linearly polarized due to the differential extinction from the alignment of asymmetric dust grains in the ISM (Hall 1949; Hiltner 1949b). The alignment process of dust grains has been a topic of discussion in the past several decades (see e.g. Davis & Greenstein 1951; Jones & Spitzer 1967; Spitzer 1978; Aannestad & Greenberg 1983; Mathis 1986; Vaillancourt, Andersson & Lazarian 2013). The paramagnetic relaxation and radiative alignment torque are the main mechanisms considered for the alignment of dust grains. In the paramagnetic relaxation mechanism, initially the grains spin after collision with hydrogen atoms and ions, and the spin axis of grains aligns with the local magnetic field by dissipation of the magnetization energy (Davis & Greenstein 1951). However, in order to align grains on time-scales faster than disruption, there are further advancements in this theory by including superparamagnetic grains, or superthermal radiation, etc. (Jones & Spitzer 1967; Purcell 1979; Mathis 1986).

The radiative torque alignment is considered to be the best alignment mechanism to explain the optical and infrared polarization (Dolginov & Mitrofanov 1976; Draine & Weingartner 1996; Lazarian & Hoang 2007). Radiative torque alignment is due to the interaction of anisotropic radiation (wavelength of radiation less than the diameter of grains) with an irregular shaped grain. Dust grains are aligned in such a way that the short axis of grains is parallel to the magnetic field. According to this theory, for a strong and anisotropic radiation field, the alignment direction can be different from the magnetic field and it may be towards the direction of radiation (Lazarian & Hoang 2007, 2021). In the majority of environments, the radiative torque alignment is a magnetic alignment in which grains are aligned along the magnetic field and the plane of the sky projection of the field can be tracked by the direction of observed polarization due to the dichroic extinction (Hoang & Lazarian 2016). Presently, all these mechanisms are being explored to support most observational findings. Thus, numerous observational results towards different directions of Galaxy are very important and play a very effective role in better understanding of the grain alignment. The polarimetric study will be an effective tool for providing information about the magnetic field orientation (Heiles 1996; Lazarian 2003, 2007), and will also reveal information about the properties of ISM dust grains and their alignment (e.g. Whittet 1992; Kim & Martin 1994; Voshchinnikov 2012; Soam et al. 2021). Dust polarization is associated with the fraction of aligned dust grains present in the ISM and how efficient the alignment will be. It is also related to the particular size and type (composition) of grains. It also depends on the magnetic field geometry along the line of sight. The correlation of polarization degree with reddening was reported by Hiltner (1949a), Hiltner (1956) with the existence of an upper limit on polarization, and in ongoing observational studies it was seen for the majority of lines of sight (e.g. Medhi et al. 2010; Singh & Pandey 2020; Singh et al.

★ E-mail: ssingh@aries.res.in (AA); jeewan@aries.res.in (JCP); thiemhoang@kasi.re.kr (TH)

2020; Vergne, Feinstein & Martínez 2007, etc.). The polarimetric study in different bands leads to information about the size of grains. The variation of polarization with wavelength is generally followed by the Serkowski relation (Serkowski, Mathewson & Ford 1975) for ISM polarization and is associated with parameters like maximum polarization (P_{max}) and wavelength (λ_{max}) corresponding to P_{max}, which is a measure of size distribution of dust grains (e.g. Kim & Martin 1994). Additionally, details of the change in the interstellar environment and magnetic fields, the existence of any dust layer, the concentration of foreground dust, etc. can be acquired.

In this paper, we present a multiband polarimetric study for an open star cluster NGC 2345. The open cluster NGC 2345 is a young cluster in Canis Major constellation ($l = 226.^{\circ}58$, $b = -2.^{\circ}31$). Distance, reddening [$E(B - V)$], and age of this cluster were estimated to be in the range of 2.2–3.0 kpc, 0.59–0.68 mag, and 55–79 Myr (in Kharchenko et al. 2005, 2013; Carraro et al. 2015; Cantat-Gaudin et al. 2018; Alonso-Santiago et al. 2019). Kharchenko et al. (2005) have derived the angular radius of core and cluster as 4.2 and 7.2 arcmin, respectively, whereas Alonso-Santiago et al. (2019) have estimated core radius of 3.44 ± 0.08 arcmin and tidal radius of 18.7 ± 1.2 arcmin for the cluster. Non radial distribution of dust associated with the cluster was noticed in various past studies with a variable reddening $E(B - V)$ from 0.4 to 1.2 mag (like Moffat 1974; Carraro et al. 2015; Alonso-Santiago et al. 2019). Carraro et al. (2015) have found variable extinction across the cluster and an overdensity was noticed upto a radius of ≈3.75 arcmin, which is a cluster radius.

The paper is organized as follows: the observations and data reduction are given in Section 2, the results and analysis are described in Section 3, whereas the discussion and summary are described in Section 4 and 5, respectively.

2 OBSERVATIONS AND DATA REDUCTION

Polarimetric observations of the cluster NGC 2345 and a field region (which is ∼1° away from the centre of NGC 2345, to increase the field population to improve statistics) were carried out on 2018 January 22, and February 14 and 15 using ARIES imaging polarimeter (AIMPOL; Rautela, Joshi & Pandey 2004), which is mounted as a back-end instrument at the 104-cm telescope (f/13 Cassegrain focus) of ARIES. The AIMPOL consists of a half-wave plate (HWP) and a Wollaston prism. HWP is rotatable and we performed observations at four different positions of HWP, i.e. 0°, $22.^{\circ}5$, 45°, $67.^{\circ}5$ from the celestial north–south direction. Through the Wollaston prism, each image is transformed into ordinary (o-) and extraordinary (e-) images on the detector. The detector used was a 1k×1k charge-coupled camera (CCD) cooled by liquid nitrogen. The read noise and gain of CCD are 7.0 e^- and 11.98 e^-/ADU, respectively. The field of view of AIMPOL is ∼8 arcmin in diameter. The observations were performed in four pass-bands: B ($\lambda_{eff} = 0.44$ μm), V ($\lambda_{eff} = 0.55$ μm), R ($\lambda_{eff} = 0.67$ μm), and I ($\lambda_{eff} = 0.80$ μm). Exposure times were 250, 200, 120, and 150 s in B, V, R, and I bands, respectively. We have taken at least three frames at each position of HWP. All frames at a position are summed in order to get a good signal-to-noise ratio. Aperture photometry was performed to get the fluxes of o- and e- images using Image Reduction and Analysis Facility.[1] Further reduction techniques are given in Singh et al. (2020). Correction for instrumental polarization was performed using an unpolarized standard star (HD21447). The instrumental polarization was found to be ≤0.3 per cent in all bands. We have observed two standard polarized stars (HD19820 and HD25443) for zero-point polarization angle correction. The observed values for polarized standard stars are found to be in good agreement with the standard values as given in Schmidt, Elston & Lupie (1992).

As there is no grid in AIMPOL, the overlapping of images can not be avoided. Thus we have manually selected the isolated sources in each B, V, R, and I bands. Owing to this and considering the offset of the observed regions in different days, we have selected 172 stars in B, 146 in V, 168 in R, and 156 in I bands. Further, we have discarded those values of a polarization for which the relative error is more than 0.5 (or $>2\sigma$). Adopting this additional criteria, we are left with 151, 132, 157, 144 stars in B, V, R, and I bands, respectively. A total of 197 sources, of which 135 are of the cluster region and 62 from the field region are included in this study. The astrometry was performed with the online available tool.[2] For the identification of observed stars, we have cross-matched our stars with the *Gaia* DR2 data sets (Gaia Collaboration 2016, 2018). Most of the stars were matched with the *Gaia* sources within 2 arcsec offset, only three stars were matched between 2 and 3.8 arcsec offset. All these sources are fulfilled by the condition for a good astrometric solution as given in Lindegren et al. (2018). Membership information of observed stars in the cluster NGC 2345 are taken from Cantat-Gaudin et al. (2018). We have considered stars as members of the cluster if the membership probability (MP) as given in Cantat-Gaudin et al. (2018) is more than 50 per cent.

3 RESULTS AND ANALYSIS

The degree of polarization (P) and polarization position angle (θ) in four bands B, V, R, and I for observed sources are given in Table 1. The source ID designated in our work is in the first column and the second column is the identification ID taken from *Gaia*. The offset from *Gaia* position is given in column 3. Then consecutive columns represent P and θ with associated errors in B, V, R, and I bands. In this table, the first 135 sources are from the cluster region and the rest 62 sources are from the field region. The member stars of the cluster NGC 2345 are marked with an asterisk symbol with their IDs.

3.1 Degree of polarization and polarization position angle

The polarization vectors in all four bands are overplotted on the DSS[3]-2-red survey images of the cluster and field regions in Figs 1 and 2, respectively. The length of the vector is proportional to the degree of polarization and their tilt denotes the position angle, which is measured from north increasing towards the east. The reference vector for 1 per cent polarization is drawn at the bottom right. The member stars of the cluster NGC 2345 are marked by the filled red circles. The dotted line in figures is the projection of orientation of Galactic parallel (GP) at both regions. The majority of polarization vectors are found to be nearly parallel to the GP in both regions. There are a few stars in both regions that are showing a larger deviation from GP.

In order to plot the distribution of P and θ, we have used the Gaussian kernel density estimation (Scott 1979; Waskom 2021a; Waskom 2021b). The density distributions along with the normalized histogram are shown in Figs 3a and b for P and θ in B, V, R, and I-bands. Hence, as position angles indicate the orientation, circular statistics are considered for showing the distribution of position angles. The majority of stars have P in the range of 0.5–2 per cent and the histogram reveals that there is no such difference between

[1] iraf.noao.edu

[2] https://nova.astrometry.net/upload

[3] http://archive.eso.org/dss/dss

Table 1. The degree of polarization (P) and position angle (θ) in the B, V, R, and I bands for all observed stars in the cluster NGC 2345 and a field region.

ID	*Gaia* ID	Offset (arcsec)	P_B (per cent)	θ_B(°)	P_V (per cent)	θ_V(°)	P_R (per cent)	θ_R(°)	P_I (per cent)	θ_I(°)
					Cluster region					
1∗	3044669369450492288	0.46	1.16 ± 0.12	162.0 ± 2.8	–	–	1.79 ± 0.12	148.9 ± 1.9	1.84 ± 0.23	160.3 ± 3.6
2	3044669369450499328	0.39	0.92 ± 0.42	119.6 ± 13.4	–	–	0.29 ± 0.11	91.4 ± 10.4	–	–
3∗	3044668380153268992	0.58	0.97 ± 0.45	154.8 ± 13.2	–	–	1.01 ± 0.13	145.8 ± 3.6	1.66 ± 0.02	155.4 ± 0.4
4∗	3044665486800115200	0.61	1.63 ± 0.19	155.4 ± 3.2	–	–	1.51 ± 0.14	154.8 ± 2.6	1.68 ± 0.38	151.7 ± 6.5
5	3044666204049384704	0.52	1.22 ± 0.24	162.8 ± 5.5	–	–	1.78 ± 0.17	145.0 ± 2.8	1.71 ± 0.06	158.8 ± 1.1
6∗	3044668682255788672	0.40	2.89 ± 0.13	139.3 ± 1.3	2.62 ± 0.01	129.4 ± 0.1	3.13 ± 0.14	137.7 ± 1.3	2.73 ± 0.03	138.8 ± 0.4
7∗	3044665727318289152	0.29	1.57 ± 0.08	145.5 ± 1.5	–	–	3.15 ± 0.18	139.9 ± 1.7	–	–
8∗	3044668819694724352	0.24	4.48 ± 1.64	163.9 ± 10.4	–	–	1.47 ± 0.12	148.2 ± 2.2	1.40 ± 0.54	165.2 ± 11.0
9∗	3044669575608944256	0.21	1.75 ± 0.02	153.1 ± 0.4	–	–	1.75 ± 0.13	146.4 ± 2.2	1.65 ± 0.11	146.9 ± 2.0
10	3044668888404742528	0.26	1.97 ± 0.04	152.9 ± 0.6	–	–	1.59 ± 0.01	150.8 ± 0.2	1.54 ± 0.15	158.2 ± 2.8
11∗	3044669541249212800	0.11	2.86 ± 0.18	129.5 ± 1.8	–	–	2.12 ± 0.01	127.9 ± 0.1	1.78 ± 0.29	129.3 ± 4.7
12∗	3044669094572631040	0.11	2.23 ± 0.04	157.9 ± 0.5	–	–	1.07 ± 0.19	152.0 ± 5.0	1.49 ± 0.30	161.3 ± 5.7
13∗	3044669163292102144	0.06	1.33 ± 0.01	154.2 ± 0.2	–	–	1.53 ± 0.14	150.1 ± 2.5	1.49 ± 0.15	153.1 ± 2.9
14∗	3044664215489824256	0.84	0.95 ± 0.17	113.5 ± 5.2	1.01 ± 0.06	133.2 ± 1.8	1.21 ± 0.09	120.3 ± 2.2	0.89 ± 0.18	134.4 ± 6.0
15∗	3044668922773965824	0.48	1.75 ± 0.08	164.7 ± 1.3	–	–	2.29 ± 0.04	155.4 ± 0.4	–	–
16	3044665761678349056	0.19	0.99 ± 0.08	11.0 ± 2.4	–	–	0.72 ± 0.04	50.9 ± 1.7	1.33 ± 0.25	27.1 ± 5.5
17∗	3044669644328400896	0.83	0.78 ± 0.01	101.2 ± 0.5	1.12 ± 0.04	138.5 ± 1.0	1.86 ± 0.06	139.7 ± 0.9	1.72 ± 0.62	135.6 ± 10.4
18∗	3044669472529743360	1.18	2.49 ± 0.17	154.8 ± 1.9	–		1.67 ± 0.22	146.6 ± 3.9	0.94 ± 0.03	139.0 ± 0.9
19∗	3044666414512997248	0.55	–	–	–	–	1.35 ± 0.07	150.9 ± 1.5	1.21 ± 0.06	164.6 ± 1.3
20∗	3044666307128599040	0.59	–	–	–	–	1.62 ± 0.04	141.7 ± 0.7	1.41 ± 0.15	145.2 ± 3.1
21	3044665967836424192	0.55	–	–	–	–	1.00 ± 0.12	140.6 ± 3.4	1.33 ± 0.12	159.1 ± 2.5
22∗	3044669266371312384	0.69	–	–	–	–	2.47 ± 0.03	164.8 ± 0.4	2.84 ± 0.22	168.5 ± 2.3
23∗	3044669266371307776	0.70	–	–	–	–	2.23 ± 0.25	170.3 ± 3.2	2.38 ± 0.21	168.3 ± 2.5
24	3044675622922858240	0.26	1.29 ± 0.24	157.2 ± 5.2	1.82 ± 0.04	154.7 ± 0.6	1.63 ± 0.09	154.4 ± 1.5	1.59 ± 0.04	158.7 ± 0.8
25∗	3044675588563126656	0.41	1.59 ± 0.06	131.9 ± 1.1	1.88 ± 0.11	127.9 ± 1.7	2.09 ± 0.03	124.6 ± 0.4	1.60 ± 0.10	161.0 ± 1.8
26	3044675588563129088	0.39	1.62 ± 0.11	12.1 ± 1.9	1.23 ± 0.17	109.7 ± 4.1	1.13 ± 0.01	145.1 ± 0.3	0.53 ± 0.07	177.6 ± 3.7
27	3044677237830539136	0.45	1.04 ± 0.33	140.6 ± 9.0	0.76 ± 0.18	142.1 ± 6.8	1.05 ± 0.02	156.2 ± 0.5	0.60 ± 0.05	136.7 ± 2.2
28∗	3044676550635786880	0.22	1.04 ± 0.01	163.0 ± 0.3	1.29 ± 0.05	152.0 ± 1.2	1.42 ± 0.22	149.8 ± 4.4	0.64 ± 0.12	146.1 ± 5.3
29∗	3044676378837101056	0.25	2.66 ± 0.41	153.8 ± 4.4	1.41 ± 0.35	147.2 ± 7.1	2.07 ± 0.02	143.5 ± 0.3	1.82 ± 0.29	149.3 ± 4.6
30	3044864532763157248	0.30	0.61 ± 0.07	167.7 ± 3.3	0.36 ± 0.04	30.9 ± 3.0	0.65 ± 0.10	3.1 ± 4.5	1.22 ± 0.08	7.5 ± 1.8
31	3044864395324215168	0.17	1.62 ± 0.18	124.0 ± 3.2	0.90 ± 0.18	165.9 ± 5.8	–	–	–	–
32∗	3044676688074753536	0.11	–	–	1.26 ± 0.18	11.3 ± 4.0	0.91 ± 0.23	176.5 ± 7.1	1.12 ± 0.04	179.6 ± 1.1
33	3044670503321866752	0.58	1.12 ± 0.04	39.7 ± 1.0	0.62 ± 0.04	51.5 ± 1.8	0.35 ± 0.02	151.3 ± 1.8	0.66 ± 0.01	13.2 ± 0.1
34∗	3044670572041356160	0.31	1.38 ± 0.18	176.1 ± 3.6	3.33 ± 0.10	159.2 ± 0.9	2.25 ± 0.03	141.5 ± 0.4	2.08 ± 0.01	149.6 ± 0.1
35	3044864734622541696	0.23	1.35 ± 0.08	43.7 ± 1.7	1.58 ± 0.04	35.5 ± 0.6	1.02 ± 0.24	30.9 ± 6.7	1.51 ± 0.23	24.9 ± 4.3
36	3044670812559502464	0.13	–	–	1.71 ± 0.10	179.5 ± 1.7	1.65 ± 0.11	165.0 ± 1.9	1.34 ± 0.25	162.5 ± 5.4
37∗	3044670675120561408	0.18	1.09 ± 0.09	165.6 ± 2.3	0.95 ± 0.30	170.1 ± 9.1	2.13 ± 0.47	164.9 ± 6.3	1.67 ± 0.24	152.5 ± 4.2
38∗	3044670572041366400	0.84	1.29 ± 0.25	138.4 ± 5.6	2.34 ± 0.61	176.8 ± 7.4	1.62 ± 0.24	140.7 ± 4.3	–	–
39∗	3044864360964480896	0.07	0.75 ± 0.17	17.2 ± 6.4	1.07 ± 0.03	177.1 ± 0.9	1.02 ± 0.07	38.0 ± 2.1	0.97 ± 0.37	178.2 ± 10.8
40∗	3044670606401093504	0.43	1.47 ± 0.09	97.7 ± 1.7	–	–	2.62 ± 0.07	166.7 ± 0.8	1.38 ± 0.28	10.2 ± 5.7
41∗	3044676756794624256	0.22	0.71 ± 0.27	175.1 ± 10.9	0.84 ± 0.21	165.6 ± 7.1	0.79 ± 0.24	174.0 ± 8.8	1.90 ± 0.52	15.9 ± 7.8
42∗	3044676447556579712	0.17	1.30 ± 0.39	143.8 ± 8.5	1.34 ± 0.09	166.8 ± 1.9	1.31 ± 0.27	167.0 ± 5.9	1.37 ± 0.04	165.7 ± 0.9
43∗	3044676340174612608	0.25	–	–	1.37 ± 0.18	157.2 ± 3.8	1.01 ± 0.03	152.0 ± 0.8	1.42 ± 0.11	165.4 ± 2.3
44	3044669713047878656	0.98	1.00 ± 0.05	137.5 ± 1.4	1.20 ± 0.18	145.0 ± 4.2	1.47 ± 0.09	129.6 ± 1.7	1.69 ± 0.12	123.3 ± 2.0
45	3044864601482633088	0.57	–	–	–	–	1.31 ± 0.24	177.1 ± 5.2	1.02 ± 0.01	148.7 ± 0.1
46∗	3044864842000808192	0.52	1.63 ± 0.02	158.9 ± 0.4	1.76 ± 0.12	166.5 ± 1.9	1.48 ± 0.11	158.9 ± 2.1	2.06 ± 0.18	156.9 ± 2.6
47	3044670537681591936	1.16	0.73 ± 0.18	51.2 ± 7.1	0.35 ± 0.05	41.2 ± 4.3	0.33 ± 0.04	55.2 ± 3.7	0.21 ± 0.08	179.9 ± 10.6
48∗	3044670503321865728	0.42	3.33 ± 0.77	69.1 ± 6.5	2.54 ± 0.03	133.3 ± 0.3	1.58 ± 0.35	122.4 ± 6.4	2.65 ± 0.62	124.3 ± 6.7
49∗	3044670400242658176	0.60	–	–	4.81 ± 0.70	141.5 ± 4.1	3.62 ± 0.04	145.2 ± 0.3	3.38 ± 0.31	136.5 ± 2.6
50∗	3044670464659348224	0.36	1.16 ± 0.25	140.7 ± 6.3	0.53 ± 0.01	145.4 ± 0.7	1.18 ± 0.36	146.1 ± 8.9	0.87 ± 0.40	155.7 ± 13.0
51∗	3044856591364735232	0.51	1.84 ± 0.11	124.5 ± 1.7	1.12 ± 0.11	123.6 ± 2.9	1.66 ± 0.10	123.5 ± 1.7	0.82 ± 0.30	121.0 ± 10.6
52	3044856458224709632	0.28	1.52 ± 0.56	25.6 ± 10.6	1.23 ± 0.11	28.9 ± 2.5	1.15 ± 0.36	50.3 ± 9.0	0.41 ± 0.10	179.1 ± 6.6
53	3044856561303914496	0.43	–	–	0.76 ± 0.13	10.2 ± 5.1	0.45 ± 0.17	39.7 ± 10.7	0.45 ± 0.01	44.8 ± 0.1
54	3044856183346803584	0.15	0.55 ± 0.07	22.1 ± 3.6	0.58 ± 0.01	14.8 ± 0.5	0.21 ± 0.05	21.1 ± 7.1	–	–
55	3044855771029950592	0.55	–	–	0.77 ± 0.07	53.0 ± 2.5	0.12 ± 0.02	10.9 ± 3.6	0.82 ± 0.07	152.2 ± 2.5
56	3044855594932139264	0.38	1.26 ± 0.18	5.5 ± 4.2	0.39 ± 0.17	171.7 ± 12.2	0.83 ± 0.12	151.6 ± 4.2	0.54 ± 0.12	174.2 ± 6.3
57	3044855736670209536	0.41	1.08 ± 0.03	15.6 ± 0.9	1.07 ± 0.19	32.8 ± 5.2	0.23 ± 0.04	65.7 ± 4.7	1.05 ± 0.23	17.9 ± 6.4
58∗	3044668059477483264	0.31	1.43 ± 0.33	134.8 ± 6.7	0.33 ± 0.13	152.3 ± 11.3	0.53 ± 0.14	110.2 ± 7.7	0.87 ± 0.20	31.7 ± 6.6
59	3044858141851970944	2.42	1.38 ± 0.27	18.4 ± 5.6	–	–	0.90 ± 0.10	5.7 ± 3.2	1.51 ± 0.41	173.4 ± 7.8
60	3044856355145484160	0.29	2.57 ± 0.41	151.6 ± 4.5	1.37 ± 0.27	176.4 ± 5.6	0.81 ± 0.34	56.1 ± 12.0	1.54 ± 0.30	34.3 ± 5.7
61	3044856217706537088	0.33	3.59 ± 0.38	126.8 ± 3.1	–	–	0.47 ± 0.12	10.9 ± 7.3	1.02 ± 0.04	11.7 ± 1.2
62	3044668579176599168	0.35	1.06 ± 0.10	15.6 ± 2.7	0.58 ± 0.02	179.8 ± 1.1	–	–	0.53 ± 0.07	12.9 ± 3.6
63	3044668407377917184	0.34	0.83 ± 0.15	14.1 ± 5.0	1.02 ± 0.01	176.5 ± 0.1	0.73 ± 0.10	166.8 ± 4.0	1.13 ± 0.01	173.1 ± 0.4
64∗	3044667720183159168	0.12	0.78 ± 0.29	175.8 ± 10.5	1.20 ± 0.08	170.7 ± 1.8	–	–	1.35 ± 0.39	119.9 ± 8.5
65	3044856286426008320	0.36	1.04 ± 0.33	171.1 ± 9.1	–	–	–	–	1.00 ± 0.22	10.3 ± 6.4
66∗	3044857832614228608	0.66	2.40 ± 0.18	126.4 ± 2.1	1.44 ± 0.62	139.6 ± 12.3	1.58 ± 0.09	132.4 ± 1.7	1.68 ± 0.51	147.0 ± 8.6
67	3044858004412908288	1.83	1.69 ± 0.06	174.4 ± 1.0	1.76 ± 0.07	174.0 ± 1.2	1.76 ± 0.12	166.0 ± 1.9	1.87 ± 0.07	171.6 ± 1.0
68∗	3044670125364791040	0.71	2.35 ± 0.27	154.8 ± 3.3	2.46 ± 0.10	150.3 ± 1.1	2.80 ± 0.21	146.5 ± 2.1	2.60 ± 0.06	153.1 ± 0.7
69∗	3044668304298684800	0.41	1.39 ± 0.01	1.0 ± 0.3	1.92 ± 0.29	166.1 ± 4.4	1.66 ± 0.05	165.2 ± 0.9	1.93 ± 0.22	169.1 ± 3.3
70	3044667479664967808	0.47	0.91 ± 0.09	163.7 ± 2.7	1.03 ± 0.06	168.6 ± 1.8	0.56 ± 0.12	135.7 ± 6.1	–	–

Table 1 – *continued*

ID	*Gaia* ID	Offset (arcsec)	P_B (per cent)	θ_B(°)	P_V (per cent)	θ_V(°)	P_R (per cent)	θ_R(°)	P_I (per cent)	θ_I(°)
71	3044669850486886912	0.69	2.29 ± 0.28	145.3 ± 3.5	1.56 ± 0.01	149.2 ± 0.1	2.05 ± 0.18	141.9 ± 2.5	1.74 ± 0.07	146.9 ± 1.2
72*	3044667445305227136	0.56	1.34 ± 0.15	174.4 ± 3.3	1.59 ± 0.35	166.9 ± 6.2	1.62 ± 0.06	168.8 ± 1.1	1.75 ± 0.16	162.7 ± 2.5
73	3044858244931080320	2.59	1.82 ± 0.01	20.1 ± 0.1	0.34 ± 0.01	159.0 ± 1.0	0.62 ± 0.10	139.6 ± 4.6	1.07 ± 0.41	8.5 ± 10.8
74	3044857832614230528	0.62	1.58 ± 0.06	145.9 ± 1.1	2.73 ± 0.06	133.7 ± 0.6	2.62 ± 0.25	136.4 ± 2.8	2.01 ± 0.17	142.3 ± 2.4
75	3044857866973962624	0.70	–	–	1.79 ± 0.12	150.3 ± 1.9	1.32 ± 0.08	140.4 ± 1.7	2.48 ± 0.78	139.2 ± 9.1
76	3044668441737656192	0.12	–	–	2.55 ± 0.51	31.7 ± 5.7	–	–	1.04 ± 0.27	25.7 ± 7.4
77	3044669747407687808	0.87	–	–	3.18 ± 0.04	153.1 ± 0.3	3.59 ± 0.16	140.8 ± 1.3	3.48 ± 0.05	143.6 ± 0.4
78	3044668132500011136	0.15	–	–	1.74 ± 0.06	170.1 ± 1.0	0.89 ± 0.05	150.3 ± 1.6	1.16 ± 0.11	159.2 ± 2.7
79	3044856355145484928	0.13	–	–	5.37 ± 0.88	127.0 ± 4.7	1.20 ± 0.11	145.2 ± 2.7	1.80 ± 0.04	138.3 ± 0.6
80	3044665349361182208	0.70	0.77 ± 0.12	3.7 ± 4.7	–	–	0.43 ± 0.05	122.9 ± 3.4	–	–
81*	3044662974233986176	0.16	0.69 ± 0.02	149.4 ± 0.8	–	–	0.74 ± 0.14	156.2 ± 5.5	–	–
82*	3044664146770344832	0.49	0.74 ± 0.07	162.2 ± 2.6	0.62 ± 0.01	7.3 ± 0.6	0.64 ± 0.17	152.6 ± 7.8	–	–
83	3044664112410613504	0.54	1.20 ± 0.32	169.1 ± 7.6	0.42 ± 0.16	14.4 ± 10.9	1.15 ± 0.05	154.0 ± 1.2	1.43 ± 0.13	158.1 ± 2.6
84*	3044664009331409152	0.46	0.57 ± 0.02	166.0 ± 0.9	1.06 ± 0.04	174.1 ± 1.0	0.90 ± 0.32	13.1 ± 10.1	–	–
85	3044663356496399360	0.13	0.50 ± 0.17	40.2 ± 9.8	0.41 ± 0.08	21.0 ± 5.4	0.34 ± 0.09	144.2 ± 7.2	–	–
86	3044663283475304576	0.30	1.02 ± 0.07	4.6 ± 2.1	0.92 ± 0.02	169.7 ± 0.8	0.94 ± 0.01	159.3 ± 0.4	–	–
87	3044663974971675008	0.37	1.24 ± 0.15	169.3 ± 3.4	1.88 ± 0.14	164.0 ± 2.2	1.21 ± 0.17	161.5 ± 4.1	1.86 ± 0.43	160.3 ± 6.5
88	3044667136067593856	1.24	0.17 ± 0.08	172.0 ± 13.1	0.54 ± 0.02	13.3 ± 1.0	–	–	0.95 ± 0.19	132.5 ± 5.8
89	3044663597014559232	0.35	0.89 ± 0.07	174.0 ± 2.1	1.13 ± 0.34	172.1 ± 8.5	0.91 ± 0.14	165.7 ± 4.4	1.23 ± 0.11	166.7 ± 2.5
90*	3044663631374306176	0.41	1.47 ± 0.26	169.4 ± 5.2	1.15 ± 0.09	173.3 ± 2.3	1.09 ± 0.09	162.2 ± 2.4	1.22 ± 0.10	169.3 ± 2.4
91*	3044667204787065216	0.18	1.52 ± 0.03	174.3 ± 0.5	0.69 ± 0.18	170.4 ± 7.3	0.82 ± 0.18	112.4 ± 6.2	–	–
92	3044667028683111296	0.40	1.23 ± 0.18	135.9 ± 4.1	0.99 ± 0.03	179.8 ± 0.8	1.13 ± 0.09	171.0 ± 2.2	–	–
93	3044666616366252160	0.43	1.38 ± 0.06	13.5 ± 1.1	0.88 ± 0.13	175.5 ± 4.1	0.42 ± 0.02	160.9 ± 1.6	–	–
94	3044666689391008768	0.19	–	–	0.82 ± 0.27	180.0 ± 9.5	–	–	0.50 ± 0.05	176.1 ± 2.7
95	3044663493935369600	0.20	–	–	0.18 ± 0.07	124.3 ± 12.1	0.46 ± 0.14	7.2 ± 8.5	1.22 ± 0.07	24.3 ± 1.6
96	3044667337920755456	0.23	–	–	4.75 ± 1.18	24.3 ± 7.1	0.58 ± 0.02	167.1 ± 1.0	0.37 ± 0.10	17.7 ± 8.1
97	3044572681146673536	0.34	–	–	0.69 ± 0.04	164.9 ± 1.5	–	–	0.73 ± 0.03	157.3 ± 1.1
98	3044667307866285568	0.41	–	–	2.03 ± 0.01	167.0 ± 0.1	1.88 ± 0.02	174.4 ± 0.2	1.85 ± 0.01	177.5 ± 0.1
99	3044663219057463808	0.53	–	–	0.68 ± 0.06	168.9 ± 2.5	1.33 ± 0.14	166.9 ± 2.9	–	–
100*	3044669506889464320	0.16	–	–	–	–	1.33 ± 0.09	153.9 ± 2.0	1.38 ± 0.14	163.2 ± 2.9
101*	3044669232011557760	0.16	–	–	–	–	1.78 ± 0.10	154.8 ± 1.6	1.51 ± 0.13	160.3 ± 2.5
102*	3044669300731031680	0.35	–	–	–	–	1.42 ± 0.12	155.2 ± 2.5	1.24 ± 0.28	166.6 ± 6.5
103*	3044665830397496576	0.16	1.21 ± 0.07	141.1 ± 1.5	–	–	–	–	–	–
104*	3044668854054467840	1.42	1.43 ± 0.33	153.9 ± 6.6	–	–	–	–	–	–
105*	3044669884846621824	0.12	2.05 ± 0.28	145.6 ± 4.0	–	–	–	–	–	–
106*	3044669987925820416	0.22	1.64 ± 0.02	128.0 ± 0.3	–	–	–	–	–	–
107*	3044670297163453824	0.37	1.34 ± 0.58	150.6 ± 12.2	–	–	–	–	–	–
108*	3044669919206348416	0.35	1.95 ± 0.12	129.8 ± 1.9	–	–	–	–	–	–
109	3044864532763156992	0.40	–	–	–	–	0.30 ± 0.12	174.8 ± 11.5	–	–
110	3044675622913302016	3.77	2.52 ± 0.65	10.0 ± 7.3	–	–	0.59 ± 0.10	159.6 ± 4.8	0.85 ± 0.16	1.8 ± 5.5
111	3044856423864969088	0.24	1.13 ± 0.23	160.3 ± 5.9	–	–	–	–	–	–
112*	3044668029420812800	0.44	0.96 ± 0.33	69.8 ± 9.8	–	–	–	–	–	–
113*	3044855736670207744	0.44	0.81 ± 0.08	178.9 ± 2.9	–	–	–	–	–	–
114	3044856217706537472	0.31	2.74 ± 0.65	176.9 ± 6.8	–	–	–	–	–	–
115	3044670052342416512	0.46	–	–	0.9 ± 0.02	6.0 ± 0.7	–	–	0.91 ± 0.26	10.0 ± 8.2
116*	3044670022285588224	0.51	2.90 ± 0.37	138.1 ± 3.7	–	–	–	–	–	–
117*	3044665589879322112	0.21	0.82 ± 0.01	122.7 ± 0.5	–	–	–	–	–	–
118*	3044665796037749632	0.33	1.31 ± 0.32	148.5 ± 6.9	–	–	–	–	–	–
119	3044665761678261760	0.30	1.33 ± 0.10	145.4 ± 2.1	–	–	–	–	–	–
120	3044663115978197504	0.15	0.69 ± 0.06	18.0 ± 2.3	–	–	–	–	–	–
121	3044662703661353600	0.55	1.32 ± 0.23	145.7 ± 4.9	–	–	–	–	–	–
122	3044662596280537600	0.88	1.45 ± 0.08	174.2 ± 1.5	–	–	–	–	–	–
123*	3044662909819779840	0.11	1.14 ± 0.21	164.6 ± 5.3	–	–	–	–	–	–
124*	3044662974235708928	0.05	–	–	–	–	0.37 ± 0.07	145.0 ± 5.8	–	–
125	3044662875460051200	1.14	1.79 ± 0.38	106.9 ± 6.1	–	–	–	–	–	–
126*	3044662871159883648	0.53	2.83 ± 1.32	93.1 ± 13.3	–	–	–	–	–	–
127*	3044663665734034688	0.36	0.79 ± 0.24	97.2 ± 8.6	–	–	–	–	–	–
128*	3044668643601838464	0.50	1.25 ± 0.19	150.1 ± 4.3	–	–	–	–	–	–
129	3044663768813248640	0.26	–	–	–	–	0.51 ± 0.12	105.2 ± 6.6	–	–
130	3044663768813249536	0.29	1.64 ± 0.21	169.3 ± 3.7	–	–	–	–	–	–
131	3044667582744222080	0.33	–	–	0.36 ± 0.07	14.2 ± 5.3	–	–	–	–
132	3044666826820729088	0.15	–	–	0.83 ± 0.02	3.5 ± 0.8	–	–	–	–
133	3044666856886407168	0.17	–	–	0.64 ± 0.16	169.4 ± 7.2	–	–	–	–
134	3044666723750771968	0.10	–	–	1.06 ± 0.39	167.3 ± 10.4	–	–	–	–
135	3044663386552561536	0.33	–	–	–	–	0.42 ± 0.19	158.0 ± 13.0	–	–
					Field region					
136	3044619994505703680	0.24	0.99 ± 0.24	157.6 ± 7.0	1.47 ± 0.68	153.8 ± 13.1	1.29 ± 0.54	142.7 ± 12.0	1.45 ± 0.07	151.3 ± 1.4
137	3044618444014605568	0.30	1.25 ± 0.14	129.9 ± 3.3	1.93 ± 0.04	156.1 ± 0.5	2.20 ± 0.22	133.3 ± 2.9	1.57 ± 0.06	139.4 ± 1.1
138	3044619685268066432	0.11	0.78 ± 0.17	145.0 ± 6.1	1.54 ± 0.34	152.2 ± 6.2	1.05 ± 0.15	142.1 ± 4.0	0.61 ± 0.05	140.5 ± 2.5
139	3044619685268070656	0.17	1.14 ± 0.52	150.5 ± 12.9	1.06 ± 0.02	153.3 ± 0.5	1.62 ± 0.10	138.9 ± 1.8	1.01 ± 0.08	139.4 ± 2.4
140	3044619616548784512	0.05	1.36 ± 0.18	176.5 ± 3.9	1.04 ± 0.21	163.4 ± 5.7	1.65 ± 0.31	143.7 ± 5.3	0.87 ± 0.10	138.1 ± 3.4

Table 1 – *continued*

ID	*Gaia* ID	Offset (arcsec)	P_B (per cent)	θ_B(°)	P_V (per cent)	θ_V(°)	P_R (per cent)	θ_R(°)	P_I (per cent)	θ_I(°)
141	3044619376030443136	0.14	2.95 ± 0.27	147.8 ± 2.6	1.74 ± 0.38	147.5 ± 6.2	1.87 ± 0.16	135.5 ± 2.5	1.92 ± 0.44	140.5 ± 6.6
142	3044623018162683136	0.20	2.25 ± 0.29	145.7 ± 3.7	2.37 ± 0.05	146.1 ± 0.6	2.00 ± 0.21	139.2 ± 3.0	1.66 ± 0.34	138.8 ± 5.8
143	3044623086882160256	0.27	2.20 ± 0.42	149.6 ± 5.4	1.27 ± 0.01	163.6 ± 0.1	0.91 ± 0.21	140.6 ± 6.5	0.95 ± 0.22	145.6 ± 6.6
144	3044619582188871808	0.09	1.58 ± 0.01	146.4 ± 0.1	1.74 ± 0.13	144.3 ± 2.1	1.51 ± 0.12	135.5 ± 2.3	1.33 ± 0.14	146.9 ± 3.0
145	3044619479109661184	0.16	–	–	2.64 ± 0.18	137.0 ± 2.0	2.44 ± 0.16	133.2 ± 1.9	2.24 ± 0.07	140.7 ± 0.9
146	3044613363076252416	0.23	0.72 ± 0.21	102.6 ± 8.1	1.32 ± 0.27	145.1 ± 5.8	1.48 ± 0.20	139.0 ± 3.8	1.16 ± 0.36	150.3 ± 9.0
147	3044623293040584064	0.36	2.21 ± 0.40	112.6 ± 5.2	1.60 ± 0.22	146.8 ± 4.0	1.90 ± 0.14	139.9 ± 2.1	1.97 ± 0.30	149.4 ± 4.4
148	3044622915083470464	0.29	0.15 ± 0.03	161.5 ± 6.0	0.40 ± 0.08	54.0 ± 5.7	–	–	–	–
149	3044622708925050496	0.06	1.59 ± 0.04	136.3 ± 0.6	1.06 ± 0.15	129.1 ± 4.1	0.70 ± 0.05	137.5 ± 1.9	0.84 ± 0.25	144.0 ± 8.5
150	3044622880723747584	0.06	3.83 ± 0.05	142.6 ± 0.4	1.99 ± 0.53	128.5 ± 7.7	2.54 ± 0.25	129.3 ± 2.8	2.09 ± 0.13	136.9 ± 1.8
151	3044619513469410176	0.39	–	–	3.80 ± 0.23	143.7 ± 1.7	2.71 ± 0.10	132.5 ± 1.1	1.77 ± 0.28	127.8 ± 4.6
152	3044616592891655808	0.20	2.13 ± 0.28	18.5 ± 3.7	0.54 ± 0.10	142.3 ± 5.2	1.02 ± 0.39	124.6 ± 10.9	–	–
153	3044622949443216896	0.29	0.73 ± 0.11	112.3 ± 4.3	–	–	0.89 ± 0.09	116.8 ± 2.8	0.57 ± 0.05	120.1 ± 2.5
154	3044623705357465216	0.15	0.63 ± 0.15	103.5 ± 6.6	0.50 ± 0.07	117.1 ± 4.0	0.55 ± 0.22	114.5 ± 11.4	0.66 ± 0.13	159.4 ± 5.7
155	3044623808436866560	0.76	1.85 ± 0.16	133.7 ± 2.5	1.57 ± 0.05	127.3 ± 1.0	1.33 ± 0.16	137.8 ± 3.5	0.78 ± 0.36	143.3 ± 13.2
156	3044623602278261120	0.09	–	–	–	–	0.67 ± 0.15	129.7 ± 6.3	1.17 ± 0.06	154.0 ± 1.5
157	3044622812004295936	0.34	1.76 ± 0.49	127.0 ± 8.1	0.89 ± 0.21	141.1 ± 6.9	1.01 ± 0.20	146.1 ± 5.6	1.09 ± 0.22	145.8 ± 5.9
158	3044616833409833984	0.19	0.84 ± 0.13	165.6 ± 4.6	1.11 ± 0.20	144.4 ± 5.2	0.88 ± 0.16	147.2 ± 5.3	1.83 ± 0.27	124.0 ± 4.2
159	3044616558531934720	1.91	1.65 ± 0.04	165.0 ± 0.7	1.03 ± 0.11	146.7 ± 3.1	1.60 ± 0.02	130.4 ± 0.3	1.84 ± 0.25	127.5 ± 3.8
160	3044613603594436224	0.24	–	–	0.28 ± 0.09	126.5 ± 9.7	–	–	1.42 ± 0.65	174.1 ± 13.1
161	3044613603594428416	0.23	1.95 ± 0.69	131.2 ± 10.2	0.89 ± 0.12	149.3 ± 3.9	0.73 ± 0.02	146.9 ± 0.7	1.83 ± 0.32	134.9 ± 5.0
162	3044622983802946176	0.58	1.69 ± 0.36	151.0 ± 6.1	1.85 ± 0.55	148.2 ± 8.4	1.94 ± 0.16	138.2 ± 2.3	1.51 ± 0.39	120.7 ± 7.2
163	3044622468406914560	1.22	3.69 ± 0.96	174.6 ± 7.4	1.53 ± 0.55	158.5 ± 10.2	2.35 ± 0.30	133.7 ± 3.7	2.06 ± 0.11	145.1 ± 1.5
164	3044616661611133696	0.41	0.95 ± 0.42	139.0 ± 12.6	1.09 ± 0.05	137.1 ± 1.4	1.08 ± 0.17	129.5 ± 4.4	0.87 ± 0.10	140.6 ± 3.1
165	3044616867769566464	0.29	1.04 ± 0.37	122.7 ± 10.2	0.54 ± 0.01	132.2 ± 0.6	0.92 ± 0.19	122.8 ± 5.9	0.40 ± 0.17	139.9 ± 12.1
166	3044626591575395840	1.24	0.23 ± 0.10	89.1 ± 11.2	–	–	0.59 ± 0.22	13.5 ± 10.5	0.34 ± 0.13	60.8 ± 10.8
167	3044626007459848576	1.25	1.08 ± 0.53	174.5 ± 20.1	1.47 ± 0.56	136.8 ± 11.3	2.09 ± 0.19	172.9 ± 2.2	2.45 ± 0.42	146.4 ± 4.9
168	3044626591575396864	1.46	2.23 ± 0.41	43.4 ± 5.7	1.84 ± 0.56	68.9 ± 8.3	1.43 ± 0.16	135.9 ± 3.5	0.88 ± 0.38	26.6 ± 12.5
169	3044625973100121984	1.03	1.34 ± 0.28	142.2 ± 6.1	1.91 ± 0.03	147.2 ± 0.4	1.56 ± 0.16	148.9 ± 2.9	1.20 ± 0.35	141.7 ± 8.4
170	3044626282338024576	1.05	0.84 ± 0.23	136.0 ± 8.4	1.75 ± 0.38	159.9 ± 5.9	1.59 ± 0.01	153.5 ± 0.2	1.16 ± 0.14	150.7 ± 3.4
171	3044626247978028672	1.14	0.65 ± 0.07	116.7 ± 3.4	–	–	1.13 ± 0.15	127.5 ± 4.2	–	–
172	3044626144898817024	1.02	–	–	0.81 ± 0.26	102.6 ± 9.0	1.48 ± 0.68	119.0 ± 14.7	1.68 ± 0.14	152.8 ± 2.4
173	3044638480044865536	0.67	–	–	3.38 ± 0.12	136.0 ± 1.1	–	–	2.17 ± 0.24	25.5 ± 3.1
174	3044638720562671488	0.41	–	–	2.28 ± 0.29	141.3 ± 3.7	2.86 ± 0.21	133.6 ± 2.4	1.97 ± 0.09	157.4 ± 1.3
175	3044626037515508096	0.65	2.07 ± 0.30	178.8 ± 3.9	2.13 ± 0.28	129.9 ± 4.1	2.57 ± 0.13	136.0 ± 1.6	2.01 ± 0.09	133.7 ± 1.3
176	3044624560046528000	0.34	0.50 ± 0.03	147.3 ± 1.6	0.67 ± 0.15	24.1 ± 6.7	0.34 ± 0.02	138.8 ± 1.4	–	–
177	3044637891625009536	1.09	–	–	0.48 ± 0.14	157.3 ± 8.1	0.94 ± 0.12	145.3 ± 3.9	1.16 ± 0.02	138.5 ± 0.4
178	3044638102087753856	0.88	1.48 ± 0.62	138.7 ± 12.7	1.86 ± 0.06	148.4 ± 0.9	1.00 ± 0.26	121.3 ± 8.3	–	–
179	3044638754922419584	1.15	1.77 ± 0.16	108.9 ± 2.7	1.12 ± 0.51	170.5 ± 21.6	3.27 ± 0.02	128.4 ± 0.2	1.22 ± 0.53	163.0 ± 12.6
180	3044638067727676800	1.31	0.90 ± 0.29	154.8 ± 8.6	1.57 ± 0.02	160.1 ± 0.3	1.57 ± 0.28	163.1 ± 4.7	1.25 ± 0.35	148.1 ± 8.1
181	3044637895929343104	1.36	6.74 ± 0.10	142.9 ± 0.4	1.78 ± 0.61	134.6 ± 10.4	1.18 ± 0.06	117.2 ± 1.7	1.51 ± 0.14	129.6 ± 2.7
182	3044624633070348288	0.77	8.24 ± 2.55	128.7 ± 10.7	1.15 ± 0.07	133.3 ± 1.9	2.06 ± 0.03	138.0 ± 0.4	0.94 ± 0.20	133.1 ± 6.0
183	3044624529991370112	0.62	–	–	–	–	1.51 ± 0.04	161.8 ± 0.6	1.50 ± 0.15	152.4 ± 2.9
184	3044638273886101888	1.42	0.75 ± 0.02	130.8 ± 0.8	1.35 ± 0.19	144.6 ± 4.2	1.43 ± 0.42	138.7 ± 9.2	0.86 ± 0.03	158.6 ± 1.0
185	3044638342605574784	1.84	3.33 ± 1.23	72.5 ± 9.5	1.08 ± 0.15	175.7 ± 3.6	2.51 ± 0.74	111.6 ± 9.1	1.34 ± 0.21	173.5 ± 4.6
186	3044638342605581056	1.97	1.28 ± 0.26	144.9 ± 5.7	1.43 ± 0.01	146.6 ± 0.1	1.38 ± 0.06	154.8 ± 1.1	1.14 ± 0.14	149.8 ± 3.5
187	3044638991136633728	2.00	0.41 ± 0.13	47.7 ± 9.6	0.33 ± 0.05	180.0 ± 3.9	0.26 ± 0.10	23.1 ± 11.4	0.41 ± 0.16	179.7 ± 11.6
188	3044638200871683968	1.49	1.48 ± 0.13	92.2 ± 2.5	0.41 ± 0.08	31.9 ± 6.1	0.23 ± 0.01	41.2 ± 0.9	0.77 ± 0.05	47.3 ± 2.0
189	3044636658978434688	0.78	1.13 ± 0.38	147.8 ± 9.4	1.62 ± 0.35	141.8 ± 6.3	2.56 ± 0.58	149.1 ± 6.5	1.84 ± 0.25	139.9 ± 3.9
190	3044636418460269184	0.67	0.99 ± 0.19	49.1 ± 5.8	1.03 ± 0.32	81.6 ± 8.5	1.01 ± 0.13	105.0 ± 3.6	0.42 ± 0.10	157.9 ± 6.9
191	3044636727697909376	0.82	2.62 ± 0.82	62.5 ± 8.3	2.32 ± 0.10	70.7 ± 1.1	1.09 ± 0.05	29.3 ± 1.6	1.36 ± 0.14	64.0 ± 3.0
192	3044636452819996032	1.29	1.06 ± 0.03	62.4 ± 0.7	0.63 ± 0.14	29.2 ± 6.6	1.06 ± 0.11	11.3 ± 2.8	0.42 ± 0.20	41.0 ± 13.4
193	3044636315381068544	1.04	1.73 ± 0.10	168.6 ± 1.6	1.92 ± 0.94	33.9 ± 14.6	1.70 ± 0.10	13.7 ± 1.6	0.80 ± 0.05	171.3 ± 1.7
194	3044626110539088896	1.07	–	–	–	–	3.43 ± 0.88	19.7 ± 7.7	1.77 ± 0.05	120.5 ± 0.8
195	3044637861569264000	0.84	3.53 ± 1.21	157.9 ± 8.7	–	–	1.98 ± 0.17	176.9 ± 2.1	1.28 ± 0.57	153.5 ± 19.5
196	3044636349740792320	0.73	1.35 ± 0.24	137.8 ± 5.4	1.64 ± 0.20	131.4 ± 3.7	1.53 ± 0.11	135.3 ± 2.3	0.97 ± 0.13	139.6 ± 3.8
197	3044624598710622464	0.57	–	–	1.38 ± 0.66	10.4 ± 13.7	–	–	0.99 ± 0.21	132.9 ± 6.0

Note. ID marked with asterisk symbol (∗) are members of the cluster NGC 2345.

the θ and the angle for GP (∼153°); however, there is a dispersion in the value of position angle in all four bands.

The plot between P_V and θ_V for all observed stars is shown in Fig. 4, in which members of NGC 2345 and field stars are shown by red triangles and black circles, respectively. For the lower polarization, there is a large dispersion in the position angles. As P_V increases, then the spread in θ_V reduces, i.e. the angle is more likely to be distributed near GP. The spread in angles is found to be more for field stars than for the cluster member stars.

3.2 Degree of polarization, position angle, and extinction as a function of distance

The foreground dust concentration towards the cluster can be inferred by exploring the polarization and/or extinction versus distance plot. The polarization is supposed to increase with the distance if dust grains are uniformly aligned. However, in some past studies, the polarization was found to rise suddenly at some distances along the line of sight of the cluster and is inferred as the presence of

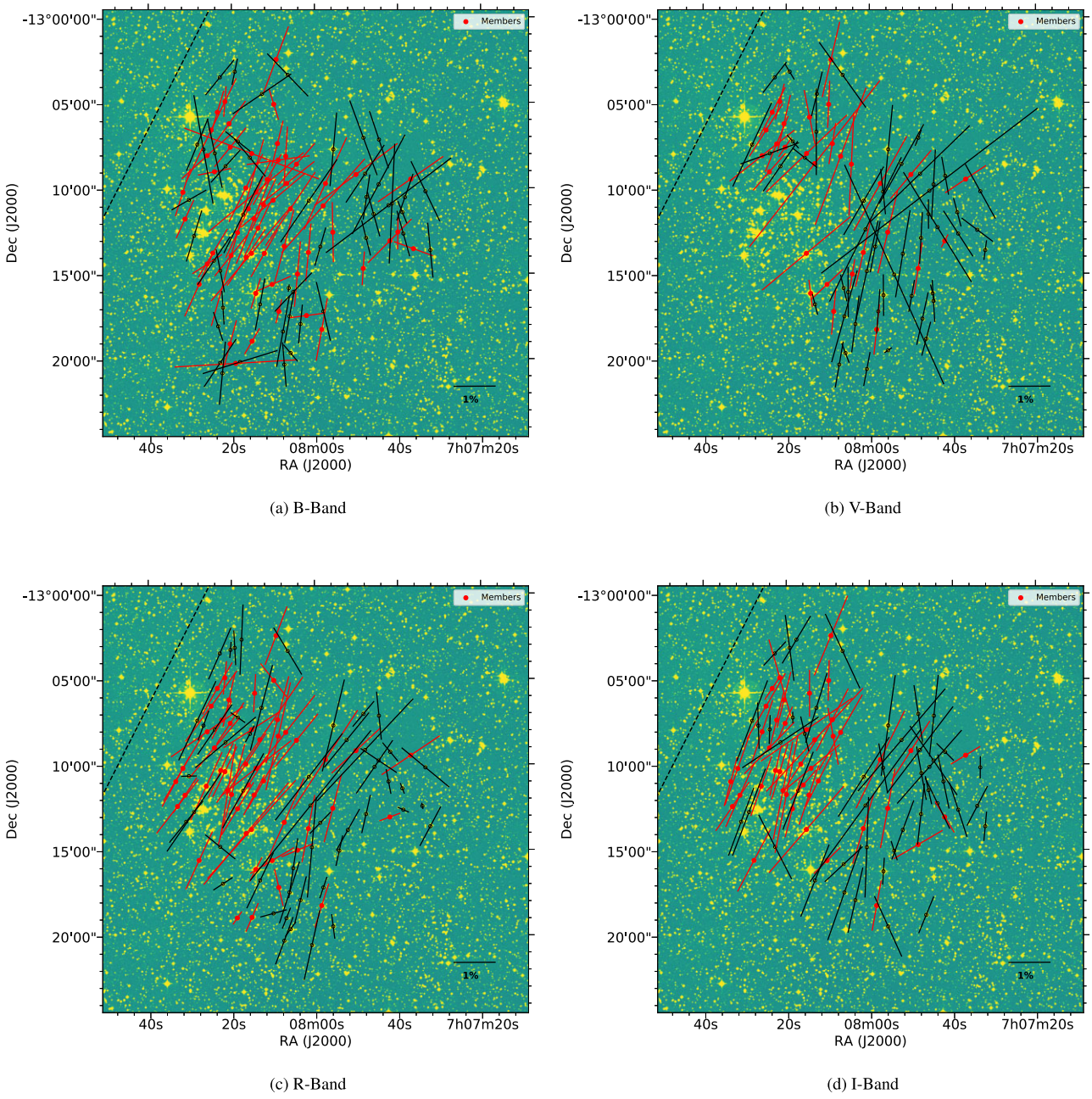

(a) B-Band

(b) V-Band

(c) R-Band

(d) I-Band

Figure 1. The polarization vectors in *B*, *V*, *R*, and *I* bands are overplotted on 25 × 25 arcmin^2 DSS *R*-band image of the cluster NGC 2345. The length of the vectors shows the degree of polarization and their tilt denotes the position angle. The reference length for 1 per cent polarization is shown at the bottom right. The dotted line denotes the orientation of the projection of Galactic Parallel in the region.

dust layers at those distances (e.g. see Vergne et al. 2007; Medhi et al. 2008, 2010; Eswaraiah et al. 2011, 2012). Vergne et al. (2010), Vergne, Feinstein & Martínez (2018) have also shown the presence of dust layer based on the jumps in extinction, but Vergne et al. (2018) did not find any rise in the polarization value at that distance.

To explore the polarization properties of dust grains at different distances, we have plotted P_V, θ_V, and extinction (A_V) as a function of distance in Fig. 5. The values of A_V of stars are taken from Anders et al. (2019). We have also taken polarization data from the catalogue of Heiles (2000) within a 5° radius of the cluster centre. A total of 43 stars were found in this catalogue, out of which the polarization values for 15 stars were within 2σ level and were not included in our analysis. Distances for stars were derived from the *Gaia* DR2 parallaxes (Gaia Collaboration 2016, 2018), for stars whose parallax values are within 2σ level were not considered for the analysis. There is an indication of a small increase in the degree of polarization at a distance of ≈1.2 kpc. We have also binned the data for distance 0.6 kpc and the average value of that bin is shown by green-filled squares in which the error bars indicate the standard deviation of that bin. After the distance of 1.2 kpc, the binned data also show a nearly constant trend. In addition to this, and as seen in Fig. 5b, a rise in the extinction from the distance ∼1.2 kpc to a distance of a cluster is noticed. We have marked the increment position in

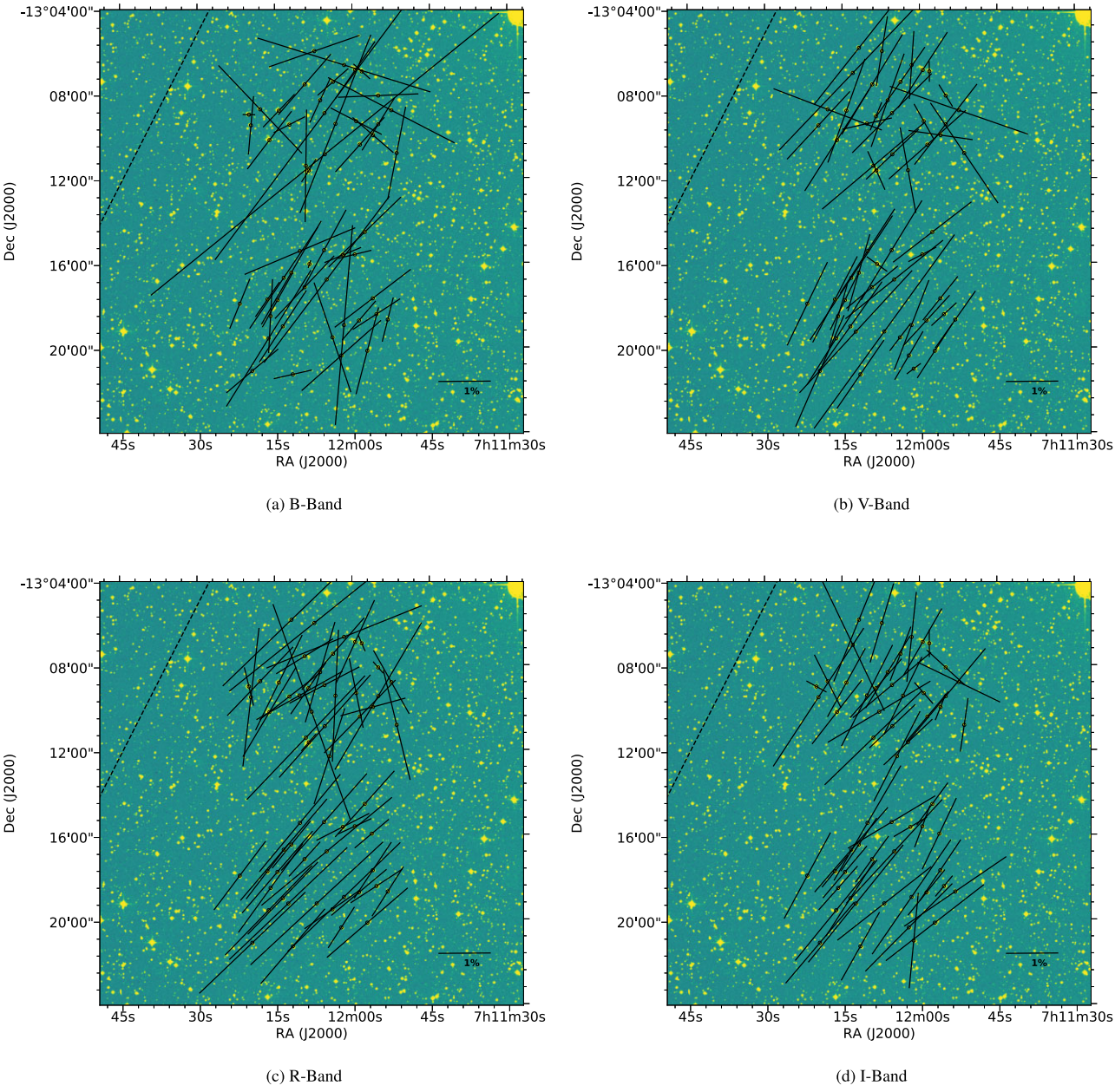

(a) B-Band

(b) V-Band

(c) R-Band

(d) I-Band

Figure 2. The polarization vectors in *B*, *V*, *R*, and *I* bands are overplotted on 20 ×20 arcmin^2 DSS *R*-band images of nearby field region of the cluster NGC 2345. The length of the vectors shows the degree of polarization and their tilt denotes the position angle. The reference length for 1 per cent polarization is shown at the bottom right. The dotted line denotes the orientation of the projection of Galactic Parallel in the region.

polarization and extinction at 1.2 kpc with the vertical magenta dotted line.

To get the enhancement in extinction after the distance of 1.2 kpc, we have fitted a Gaussian curve to the distribution of A_V for $d \leq 1.2$ and $d > 1.2$ kpc, which reveals an average increase of ∼1.15 mag in extinction after the distance 1.2 kpc. From Fig. 5c, it can be seen that, stars located before the distance of ∼1.2 kpc generally show more dispersion in position angle, whereas after ∼1.2 kpc, the position angle is distributed towards the GP direction with small spread. It can be clearly seen that as the distance increases after 1.2 kpc, the θ_V tends to decrease. The increment in the polarization and extinction after the distance ∼1.2 kpc towards the direction of the cluster NGC 2345 could be due to the enhancement and/or change in the distribution of dust grains.

3.3 Wavelength-dependence polarization

The wavelength dependence of ISM polarization follows the relation (Serkowski 1973; Serkowski et al. 1975),

$$P_\lambda = P_{\max} \exp[-1.15 \ln^2(\lambda_{\max}/\lambda)], \quad (1)$$

where P_λ is the polarization at wavelength λ, $P_{\max}$ is the maximum polarization and $\lambda_{\max}$ is the wavelength corresponding to $P_{\max}$. The $\lambda_{\max}$ is a function of optical properties and characteristic particle size distribution of aligned grains. The relation provides the observed variation of ISM polarization with a wavelength between the range of 0.36–1 μm (Wilking, Lebofsky & Rieke 1982; Whittet et al. 1992; Eswaraiah et al. 2012; Pandey et al. 2013). Using the above relation, we have estimated the parameters $P_{\max}$ and $\lambda_{\max}$ of those stars for

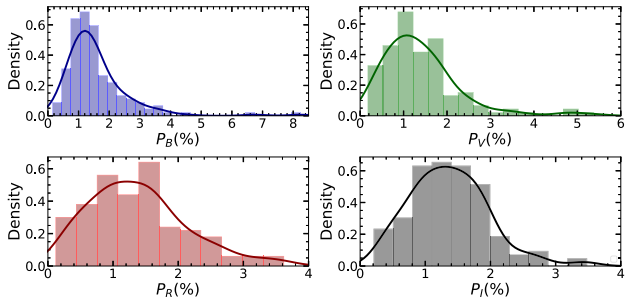

(a) The distribution of P among observed stars.

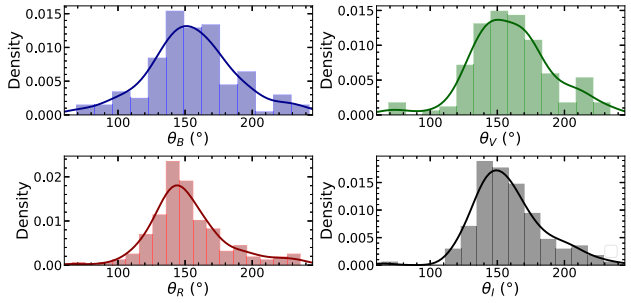

(b) The distribution of θ.

Figure 3. (a, b) The distribution of P and θ of observed stars. The blue, green, red, and black colours show the distributions in the B, V, R, and I bands, respectively. The Gaussian kernel density estimation is shown by the blue, green, red, and black curves for B, V, R, and I bands, respectively.

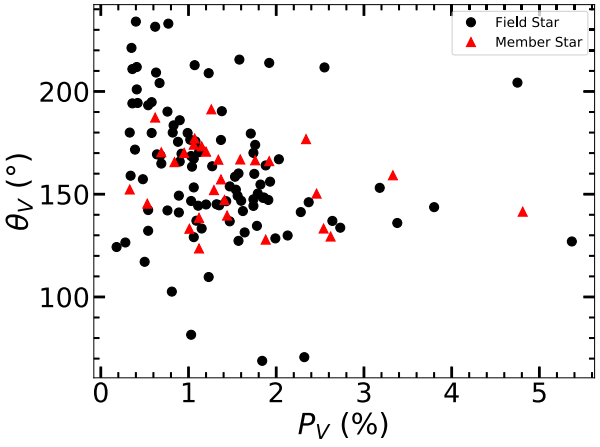

Figure 4. The plot of P_V versus θ_V. Member stars of the cluster NGC 2345 are shown by the red-filled triangle, and all other observed stars in the study are shown by the black-filled circle.

which the data are available in at least three bands. We have computed the parameter σ_1 (unit weight error of fit), which quantifies the departure of data from the relation 1. The polarization is considered intrinsic in origin if $\sigma_1 > 1.6$ (Waldhausen, Martínez & Feinstein 1999; Vergne et al. 2007; Medhi et al. 2008; Pandey et al. 2013; Singh & Pandey 2020). Even if the relation 1 fits well to the data, it is not necessary that the polarization is due to the ISM. There may be chances of another origin of polarization, e.g. circumstellar shells follow a different wavelength dependency on polarization than the ISM one, which could resemble the interstellar law in a limited range of wavelength (Orsatti, Vega & Marraco 1998). Thus, stars with the

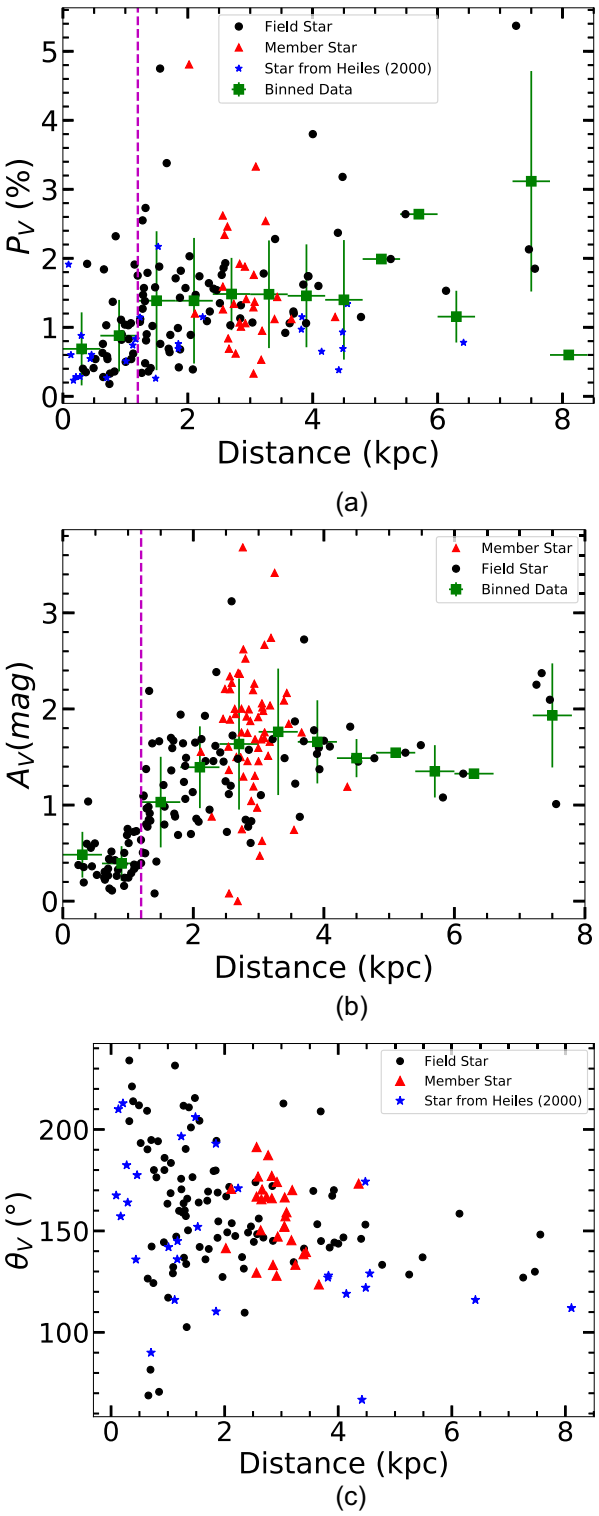

Figure 5. (a) Variation of degree of polarization in V-band with distance. The data have been binned for 0.6 kpc distance and shown by green-filled squares and error denotes the standard deviation. The magenta dotted vertical line at 1.2 kpc denotes the increment in polarization. (b) Variation of A_V with distance. Red triangles are marking members. And binned data are shown for the 0.6 kpc binning scheme. (c) θ_V versus distance. Red triangles are for members; blue asterisks are stars taken from Heiles (2000); and black circles are for all other observed stars.

Table 2. The values of P_{max}, λ_{max}, and σ_1 as obtained after best fit of the Serkowski relation.

ID	P_{max} (per cent)	λ_{max} (μm)	σ_1	ID	P_{max} (per cent)	λ_{max} (μm)	σ_1
1	1.88 ± 0.03	0.84 ± 0.02	0.1	90	1.20 ± 0.09	0.62 ± 0.12	0.7
4	1.67 ± 0.12	0.53 ± 0.07	0.5	92	1.05 ± 0.17	0.66 ± 0.27	0.9
5	1.73 ± 0.03	0.74 ± 0.04	0.2	93	4.57 ± 0.70	0.16 ± 0.01	0.3
6	2.79 ± 0.08	0.69 ± 0.04	1.5	98	2.03 ± 0.05	0.59 ± 0.03	0.9
9	1.87 ± 0.02	0.56 ± 0.01	0.2	136	1.45 ± 0.02	0.78 ± 0.04	0.2
10	1.97 ± 0.07	0.44 ± 0.02	0.6	137	1.88 ± 0.11	0.57 ± 0.08	1.1
11	2.88 ± 0.09	0.40 ± 0.01	0.2	138	0.96 ± 0.31	0.44 ± 0.12	1.0
12	2.56 ± 0.62	0.31 ± 0.09	1.2	139	1.17 ± 0.20	0.73 ± 0.20	1.1
13	1.56 ± 0.02	0.64 ± 0.01	0.1	140	1.31 ± 0.23	0.45 ± 0.08	0.8
14	1.11 ± 0.09	0.69 ± 0.12	0.4	141	2.91 ± 0.63	0.36 ± 0.07	0.9
16	0.98 ± 0.28	0.41 ± 0.13	1.5	142	2.44 ± 0.08	0.46 ± 0.03	0.3
17	2.74 ± 0.60	1.25 ± 0.12	0.7	143	1.77 ± 0.77	0.32 ± 0.11	0.8
18	3.07 ± 0.48	0.29 ± 0.02	0.6	144	1.64 ± 0.02	0.53 ± 0.02	0.2
24	1.80 ± 0.05	0.57 ± 0.03	0.6	145	2.61 ± 0.07	0.55 ± 0.02	0.2
25	2.04 ± 0.08	0.68 ± 0.07	0.9	146	1.49 ± 0.30	0.88 ± 0.19	0.5
26	1.85 ± 0.56	0.35 ± 0.07	0.9	147	1.90 ± 0.15	0.64 ± 0.16	0.8
28	1.16 ± 0.15	0.59 ± 0.11	1.0	149	2.47 ± 0.33	0.24 ± 0.02	0.6
29	2.21 ± 0.35	0.53 ± 0.16	1.1	150	3.95 ± 0.17	0.37 ± 0.03	1.3
32	1.20 ± 0.15	0.62 ± 0.14	0.6	151	6.35 ± 0.42	0.28 ± 0.01	0.1
34	2.45 ± 0.39	0.55 ± 0.10	2.5	153	0.81 ± 0.19	0.49 ± 0.12	0.6
35	1.58 ± 0.09	0.61 ± 0.10	0.8	154	0.60 ± 0.10	0.72 ± 0.19	0.4
36	1.72 ± 0.05	0.53 ± 0.04	0.2	155	1.90 ± 0.12	0.37 ± 0.02	0.2
37	1.68 ± 0.31	0.82 ± 0.13	0.8	157	1.08 ± 0.19	0.58 ± 0.23	0.9
38	1.68 ± 0.31	0.68 ± 0.21	1.0	158	1.28 ± 0.45	0.85 ± 0.31	1.0
39	1.07 ± 0.03	0.60 ± 0.08	0.4	159	1.68 ± 0.10	0.54 ± 0.07	1.5
40	2.71 ± 0.75	0.88 ± 0.28	2.5	162	2.04 ± 0.57	0.92 ± 0.33	0.8
42	1.41 ± 0.02	0.68 ± 0.02	0.2	163	2.36 ± 0.51	0.56 ± 0.16	1.3
44	1.62 ± 0.08	0.85 ± 0.04	0.3	164	1.09 ± 0.02	0.52 ± 0.02	0.2
46	1.77 ± 0.13	0.57 ± 0.07	1.0	166	0.39 ± 0.14	0.82 ± 0.33	0.5
47	0.54 ± 0.26	0.33 ± 0.12	0.4	167	2.80 ± 0.15	1.11 ± 0.05	0.1
48	3.17 ± 1.32	0.35 ± 0.15	1.2	168	2.47 ± 0.21	0.33 ± 0.02	0.2
49	3.94 ± 0.76	0.51 ± 0.16	1.2	169	1.93 ± 0.15	0.48 ± 0.12	0.9
51	1.65 ± 0.35	0.46 ± 0.17	1.3	170	1.59 ± 0.04	0.65 ± 0.21	1.0
53	0.86 ± 0.25	0.38 ± 0.06	0.3	172	2.65 ± 0.50	1.50 ± 0.19	0.3
63	1.13 ± 0.02	0.75 ± 0.03	0.9	174	2.71 ± 0.93	0.48 ± 0.16	1.2
64	1.44 ± 0.20	0.83 ± 0.12	0.3	175	2.41 ± 0.22	0.56 ± 0.08	0.7
66	2.48 ± 0.27	0.36 ± 0.03	0.7	176	0.52 ± 0.08	0.36 ± 0.05	0.6
67	1.91 ± 0.07	0.64 ± 0.04	0.5	177	1.90 ± 0.58	1.54 ± 0.31	0.3
68	2.67 ± 0.04	0.69 ± 0.03	0.4	179	3.83 ± 1.10	0.97 ± 0.32	2.8
69	1.69 ± 0.06	0.66 ± 0.03	0.6	180	1.62 ± 0.16	0.65 ± 0.16	0.7
70	1.00 ± 0.25	0.43 ± 0.19	0.8	184	0.91 ± 0.04	0.66 ± 0.04	1.0
71	1.75 ± 0.17	0.75 ± 0.10	1.5	185	1.36 ± 0.39	0.81 ± 0.34	1.8
72	1.65 ± 0.04	0.70 ± 0.05	0.3	186	1.43 ± 0.01	0.55 ± 0.02	0.2
74	2.84 ± 0.84	0.81 ± 0.23	1.9	187	0.35 ± 0.06	0.48 ± 0.17	0.3
77	3.51 ± 0.03	0.74 ± 0.01	0.3	189	1.93 ± 0.23	0.81 ± 0.15	0.7
82	0.76 ± 0.12	0.36 ± 0.06	0.4	190	1.16 ± 0.47	0.36 ± 0.11	0.6
85	0.50 ± 0.04	0.37 ± 0.03	0.1	192	1.06 ± 0.08	0.43 ± 0.12	0.9
86	0.95 ± 0.03	0.59 ± 0.07	0.6	193	1.92 ± 0.55	0.36 ± 0.08	1.2
87	1.57 ± 0.24	0.60 ± 0.21	1.0	195	4.34 ± 0.41	0.29 ± 0.01	0.1
89	1.15 ± 0.11	0.72 ± 0.09	0.5	196	1.60 ± 0.26	0.47 ± 0.09	0.6

value of λ_{max} considerably smaller or larger than the average value for general ISM (0.55 μm), may be considered as intrinsically polarized (Serkowski et al. 1975; Orsatti et al. 1998; Vergne et al. 2007; Medhi et al. 2010; Singh & Pandey 2020; Singh et al. 2020)

The derived values of P_{max}, λ_{max}, and σ_1 for 100 stars are given in Table 2, where stars' IDs are same as in Table 1. In this table, we have only given those stars for which the values of P_{max} and/or λ_{max} are determined above 2σ level. Based on σ_1 criteria, we found that five stars (ID: 34, 40, 74, 179, and 185) have an intrinsic component of polarization. For the ISM originated polarization the value of λ_{max} should be in the range of 0.45–0.8 μm (Serkowski et al. 1975). For 19 stars (ID: 11, 12, 18, 26, 53, 66, 82, 85, 93, 141, 143, 149, 150, 151, 155, 168, 176, 193, and 195), the value of λ_{max} is found to be significantly less than 0.45 μm, whereas for six stars (ID: 1, 17, 44, 167, 172, and 177), λ_{max} is found to have significantly higher value than 0.8 μm. Thus, there are a total of 30 stars which may also have an intrinsic component of polarization. Two stars (ID 11 and 82) are reported as blue stars in Stephenson & Sanduleak (1971), Moffat (1974), Alonso-Santiago et al. (2019) and there is a probability for the presence of significant component of intrinsic

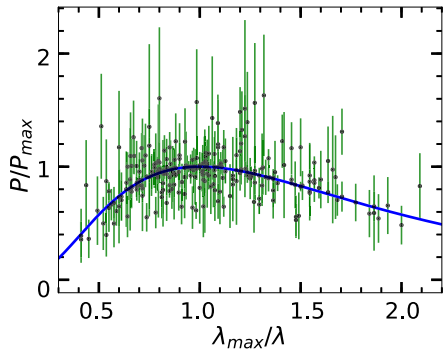

Figure 6. Normalized wavelength-dependence-polarization plot for observed stars, intrinsically polarized stars are excluded from the plot. The blue curve shows the Serkowski relation.

polarization in blue stars (Coyne & Kruszewski 1969; Capps, Coyne & Dyck 1973; Haisch & Cassinelli 1976; Poeckert & Marlborough 1978). Excluding all intrinsically polarized stars, the average value of λ_{max} and P_{max} were determined after Gaussian fitting to their distribution and found to be 0.58 ± 0.13 μm and 1.55 ± 0.47 per cent, respectively, where the error in each parameter is standard deviation. The plot between λ_{max}/λ and P/P_{max} is shown in Fig. 6, where the blue curve shows the Serkowski relation for general ISM. The value of λ_{max} is associated with the average size of ISM dust grains (Serkowski 1968, 1973) and is estimated to be around 0.55 μm for general ISM. This indicates that the average size distribution of dust grains towards the direction of NGC 2345 is similar to that of general ISM.

3.4 Polarizing efficiency

The polarizing efficiency is a measure of the polarization produced by a given amount of extinction (i.e. the ratio of polarization to the reddening or extinction). Polarizing efficiency depends upon the magnetic field orientation, strength, and alignment efficiency (Voshchinnikov & Das 2008; Voshchinnikov 2012; Voshchinnikov et al. 2012). Thus, different regions of Galaxy, e.g. molecular clouds, diffuse ISM, and star-forming regions, etc., show different behaviour of polarizing efficiency. Fig. 7 shows the polarizing efficiency plots for the observed region NGC 2345. For the diffused ISM, the maximum polarization for a given extinction can be limited by $P_{max} \leq 3R_V \times E(B-V)$ (Hiltner 1956; Serkowski 1973; Serkowski et al. 1975). The black straight line in Fig. 7a corresponds to the maximum polarization with total-to-selective extinction (R_V) as 3.1. Polarizing efficiency for the majority of stars is found to be below the maximum efficiency for the region NGC 2345. There are only a few stars that show the polarizing efficiency more than the maximum value expected for the region, which could be due to the intrinsic nature of polarization in these stars. The blue dotted curve in Fig. 7a shows the average value of polarizing efficiency of the Galaxy which is estimated by using the relation $P = 3.5 \times E(B-V)^{0.8}$ for $E(B-V) <$ 1.0 mag (Fosalba et al. 2002). It is seen from this figure that the values of polarization for the majority of cluster members were found to be less than the average value for the Galaxy. The majority of cluster members lie below the average efficiency curve (dashed blue curve). However, the majority of field stars lie in between the maximum estimated value and the average value of polarizing efficiency for the Galaxy. This analysis further indicates that polarization and polarizing efficiency in observed regions are similar to the general ISM.

The alignment of grains in the region can be examined by the behaviour of polarizing efficiency with extinction. A number of studies (e.g. Jones, Klebe & Dickey 1992; Whittet et al. 1994, 2001, 2008; Alves et al. 2014; Andersson, Lazarian & Vaillancourt 2015; Hoang, Lazarian & Andersson 2015; Jones et al. 2015; Wang et al. 2017; Il'in et al. 2018; Medan & Andersson 2019; Soam et al. 2021) have found reducing polarizing efficiency with extinction, which follows the power-law relation $P_{max}/A_V = \beta(A_V)^{\alpha}$ with power-law index, α close to -0.5. For the inner region of the clouds, the value of α near -1 denotes the total loss of grain alignment that occur for $A_V \gtrsim 20$ mag (Jones et al. 2015). We have also fitted the power law, which yields the relation $P_{max}/A_V = (1.39 \pm 0.09)(A_V)^{-0.67 \pm 0.09}$ for the region of the cluster NGC 2345. We used the bootstrap method (Efron 1979; Efron & Tibshirani 1994) to estimate the value of the power-law index and corresponding error. In the bootstrap method, the sample statistics are determined using random sampling with replacement, which increases the accuracy of sample estimates. The re-sampling is carried out 2000 times with a similar sample size as data points and replacement. The power-law fit is performed for each sample, and the mean value of fitting parameters with the standard deviation is calculated. Fig. 7b shows the variation of P_{max}/A_V with A_V along with the best fit power law. Here, for better representation, the data and corresponding best-fitting power-law are converted into the log–log scale.

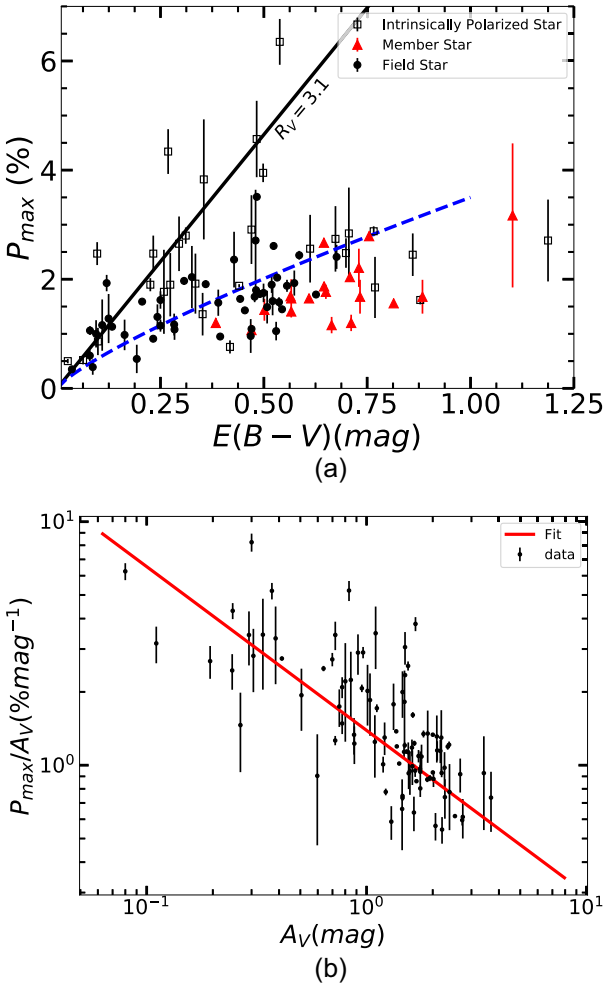

Figure 7. The polarizing efficiency diagram. (a) The variation of P_{max} with reddening $E(B-V)$. The black line shows the line for maximum efficiency for R_V =3.1, while the blue curve signifies average efficiency estimated for Galaxy. (b) P_{max}/A_V as a function of A_V. The red line shows the best-fitting power law to the data in the log–log scale using the bootstrap sampling method.

The distribution of P_{max}/A_V and λ_{max} with the radial distance from the centre of cluster NGC 2345 are shown in Fig. 8. Intrinsically polarized stars are not included in this plot. The data have been binned for ∼1.25 arcmin along the radial direction. The binned data are shown by blue squares. Each bin value is the weighted average of the parameter in that bin, and the weighted standard deviation is shown by error bars. The P_{max}/A_V was found to be decreasing from centre to outwards of the cluster NGC 2345. A higher value of P_{max}/A_V is seen in the core region with respect to the coronal region of the cluster. Whereas an increasing trend in the value of λ_{max} was found from core region to outwards.

3.5 Wavelength of maximum polarization as function of extinction and polarizing efficiency

Whittet & van Breda (1978) showed a relation between R_V and λ_{max} as $R_V = 5.6 \times \lambda_{max}$. However, in the later studies, it was found that no clear trend of increasing R_V with λ_{max}, but a clustering around the value of λ_{max} near 0.55 µm in some studies (e.g. Clayton & Mathis 1988; Whittet et al. 1994, 2001; Andersson & Potter 2007) was noticed. The poor correlation between these two parameters was considered to be due to the size dependent variation in grain alignment, as λ_{max} is related to size of those grains which are aligned. It was found that the relation between λ_{max} and R_V gives a meaningful estimation for extinction larger than ice threshold extinction ($A_V = 3.2$) (Whittet et al. 2001). Further, a marginal correlation between λ_{max} and A_V was found (e.g. in studies Whittet et al. 2001; Andersson & Potter 2007; Whittet et al. 2008; Il'in et al. 2018; Vaillancourt et al. 2020). We have shown the dependence of λ_{max} on A_V in Fig. 9a for observed region NGC 2345. The members of cluster NGC 2345 are shown by red-filled triangles, while other field stars are marked by black-filled circles, and stars that are found to be intrinsically polarized from Section 3.3 are shown by black squares. The blue line represents the best fit straight line using the bootstrap sampling method as described in Section 3.4. The best fit straight line shows the relation of $\lambda_{max} = (0.09 \pm 0.05) \times A_V + (0.35 \pm 0.09)$. However, the linear relation between λ_{max} and A_V is not statistically significant.

Fig. 9b shows the variation of λ_{max} with P_{max}/A_V. It shows that with the increase in P_{max}/A_V, λ_{max} decreases. A similar trend was also found by Whittet et al. (2001), Andersson & Potter (2007), Voshchinnikov (2012), Voshchinnikov, Il'in & Das (2016), Il'in et al. (2018).

4 DISCUSSION

A polarimetric study of a total of 197 sources of the cluster NGC 2345 and a nearby field region has been carried out. The polarization is found to be wavelength dependent for majority of stars with the average value of $\lambda_{max} \approx 0.58$ µm and $P_{max} \approx 1.5$ per cent. No distinction in the distribution of degree of polarization was observed between cluster members and other observed stars. Below, we discuss our results based on our findings.

4.1 Orientation of dust grains towards the cluster

The polarization vectors for the majority of stars in both cluster and field regions are found to be parallel to the GP. The parallelism of polarization vectors with the GP indicates that dust grains are aligned with the Galactic magnetic field in both regions. There are a few stars for which the polarization vectors are not parallel to the GP. We have also noticed the change in the polarization properties along with the increment of visual extinction near the

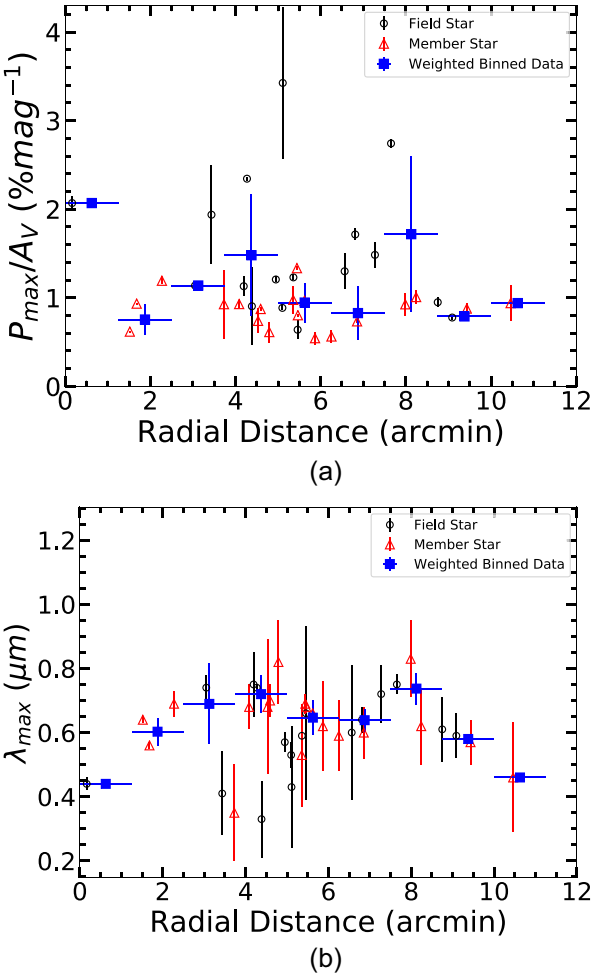

Figure 8. The distribution of P_{max}/A_V and λ_{max} with the radial distance from the centre of the cluster NGC 2345. The data have been binned for ∼1.25 arcmin along the radial direction, where each bin value is the weighted average of the parameter in that bin and error bars show the weighted standard deviation.

distance of 1.2 kpc. Majority of stars with a larger deviation of θ_V from GP are found to lie before this distance (see Section 3.2). Also, while going away from the distance of 1.2 kpc, the values of θ_V are found to be similar to GP direction. Relatively smaller dispersion in θ_V for cluster members shows the better alignment of dust grains in the intra-cluster medium. It shows that there is a presence of different orientations of dust polarization (other than GP) for the foreground in the cluster region, which causes a spread in position angles. It appears that grains beyond 1.2 kpc distance are aligned with the Galactic magnetic field. However, foreground dust may have a magnetic field significantly different from the GP. The magnetic field orientation in the foreground is not as organized as in the cluster region. Additionally, the decreasing trend of θ_V with distance beyond the distance of 1.2 kpc reveals the spatial variation of the magnetic field over different scales.

4.2 Implications for grain alignment mechanisms

The differential dust concentration in the cluster region is also observed. We have found a decreasing trend of polarizing efficiency with the radial distance of the cluster, which shows the increased alignment efficiency towards the cluster centre. In previous studies

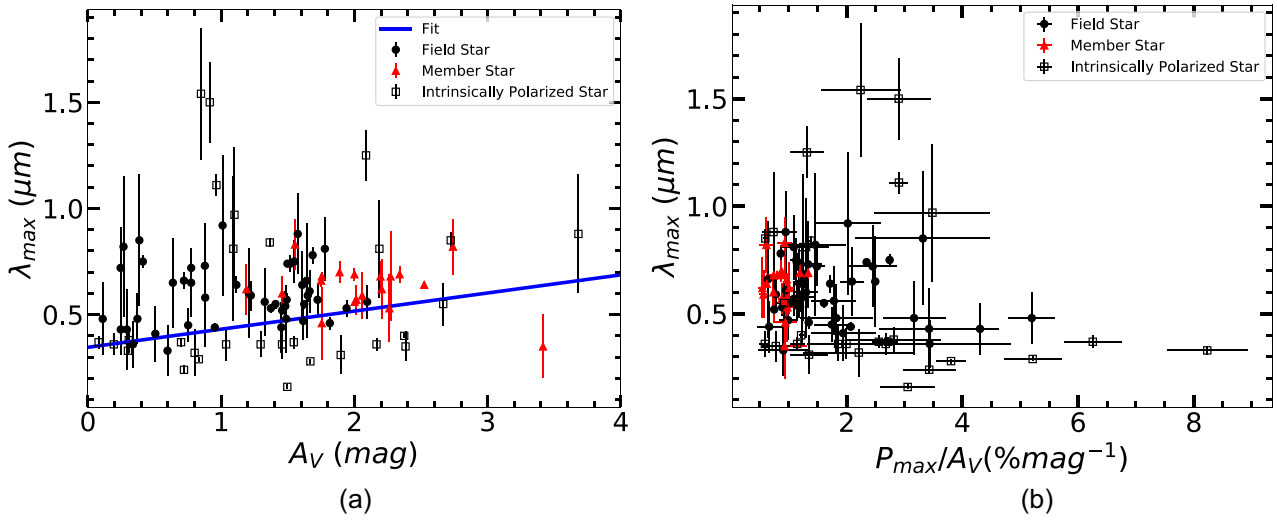

Figure 9. (a) Variation of λ_{max} with A_V. The data have been fitted with a straight line, represented by the blue line. (b) The variation of λ_{max} with the polarizing efficiency for the observed region.

of the cluster NGC 2345, it was found that the cluster is affected by differential reddening with the variation of $E(B-V)$ is from 0.5 to 1.2 mag with the average value of 0.66 ± 0.13 mag (Moffat 1974; Carraro et al. 2015; Alonso-Santiago et al. 2019). We have noticed that P_{max} in the core region of the cluster is higher than that in the coronal region, which is similar to that we found for the $E(B-V)$ values. In addition to this, no specific variation of θ_V with the radial distance is seen, which implies that the orientation of the alignment factor is not much changing inside the cluster. The decreasing trend of λ_{max} towards the cluster centre shows that the average size of aligned grains reduces towards the centre of the cluster NGC 2345. The observed polarizing efficiency [$P_{max}/E(B-V)$] for the majority of field stars is found to be more than the estimated value for the Galaxy, whereas the polarizing efficiency for cluster members is found to be similar or less than that of the estimated average value for the Galaxy (see Fosalba et al. 2002). Also, the estimated average values of polarizing efficiency of the Galaxy of 3.8 per cent/mag is found to be in between to that of the average value for the field and member stars of 5.5 and 2.9 per cent/mag, respectively. The lower polarizing efficiency of cluster members indicates the less polarizing efficiency of the intra-cluster medium. It seems that starlight from cluster members has been depolarized due to the nonuniform alignment of dust grains in the foreground and intra-cluster medium. The dispersion in P_{max} for cluster members is compatible with the differential reddening in the cluster. Similar results were found by Eswaraiah et al. (2012); Pandey et al. (2013). Polarizing efficiency (P_V/A_V) is found to follow a power law relation with extinction, A_V with a slope of −0.67. Differences in alignment of grains, grain properties (size), and magnetic fields can cause variation in P_V/A_V and different slopes (α) from region to region. There have been studies of different regions of ISM with similar power law behaviour (e.g. in Goodman et al. 1992; Gerakines, Whittet & Lazarian 1995; Whittet et al. 2008; Alves et al. 2014; Andersson et al. 2015; Hoang et al. 2015; Jones et al. 2015; Soam et al. 2021), whereas for a few lines of sight, α was found relatively higher (Goodman et al. 1995; Whittet et al. 2001; Cashman & Clemens 2014; Wang et al. 2017; Il'in et al. 2018; Medan & Andersson 2019) showing lesser efficiency of grain alignment at higher extinction. According to Jones et al. (1992), the slope of ∼−0.5 for moderate extinction is expected due to the effect of magnetic field turbulence.

The slope of λ_{max} and A_V relation in our study is found similar to that found by Whittet et al. 2008; Il'in et al. 2018. However, in some studies Andersson & Potter (2007); Vaillancourt et al. (2020), a relatively smaller slopes (≈0.03) were found. According to radiative alignment theory, grains are aligned when anisotropic radiation is sufficiently strong to spin-up grains to superthermal rotation (Hoang et al. 2021). Hence, with the increase in A_V, the aligning radiation becomes weaker and the gas density is higher, so that only larger grains with larger radiative torque efficiency can be aligned, corresponding to the increase in the size of the smallest aligned grains (Hoang et al. 2021). Therefore, the increase of λ_{max} with A_V is expected. Additionally, we have found the decreasing trend of λ_{max} with the increase in P_{max}/A_V which shows with the increase in P_{max}/A_V (i.e. larger efficiency of alignment), the average size of aligned dust grains reduces. It suggests that smaller grains are also aligned with the larger alignment efficiency so the average size of aligned grains shifted towards a smaller value, while for lower alignment efficiency, relatively larger grains are aligned, so the average size is large as a result λ_{max} show higher value. Our results shown in Fig. 8 reveal an overall increase of P_{max}/A_V and decrease of λ_{max} toward the cluster center. This may be caused by the increase in the local radiation field due to stars within the cluster that increases the alignment efficiency of small grains, following the radiative torque alignment theory (Hoang et al. 2021).

5 SUMMARY AND CONCLUSIONS

Using the polarimetric observations of 197 stars in the cluster NGC 2345 and field regions, we have found a single distribution of degree of polarization and position angles. The majority of polarization vectors are found nearly parallel to the direction of Galactic parallel indicating the alignment of dust grains possibly with the Galactic magnetic field. An increment in the dust concentration seems to occur with A_V of ∼1.15 mag near the distance of 1.2 kpc towards the line of sight, which is also accompanied by the change in polarization properties. The variation of polarization with wavelength is fitted by the Serkowski empirical relation, yielding the maximum value of polarization and its corresponding wavelength as 1.55 per cent and 0.58 μm, respectively. This indicates that the polarization in the direction is due to the foreground ISM and that the average

size distribution of dust grains is similar to the general ISM dust grains. The increment of wavelength for maximum polarization with extinction accompanied by its decrements with increasing polarizing efficiency, could be a result of radiative torque alignment of grains. The increasing polarizing efficiency and decreasing wavelength of maximum polarization towards the cluster centre indicates about increasing local radiation field within the cluster, which supports the radiative torque alignment theory.

ACKNOWLEDGEMENTS

We thank the referee for his/her useful comments and suggestions. Part of this work has made use of data from the European Space Agency (ESA) mission *Gaia* (https://www.cosmos.esa.int/gaia), processed by the *Gaia* Data Processing and Analysis Consortium (DPAC, https://www.cosmos.esa.int/web/gaia/dpac/consortium). Funding for the DPAC has been provided by national institutions, in particular the institutions participating in the *Gaia* Multilateral Agreement. TH acknowledges the support by the National Research Foundation of Korea (NRF) grants funded by the Korean government (MSIT) through the Mid-career Research Program (2019R1A2C1087045). SS acknowledges Biman J Medhi for his support in initiating the project, Archana Soam for reading initial draft version of the paper, and Priyanka Srivastava for help during observations.

DATA AVAILABILITY

The data underlying this article are available in the article.

REFERENCES

Aannestad P. A., Greenberg J. M., 1983, ApJ, 272, 551
Alonso-Santiago J., Negueruela I., Marco A., Tabernero H. M., González-Fernández C., Castro N., 2019, A&A, 631, A124
Alves F. O., Frau P., Girart J. M., Franco G. A. P., Santos F. P., Wiesemeyer H., 2014, A&A, 569, L1
Anders F. et al., 2019, A&A, 628, A94
Andersson B. G., Potter S. B., 2007, ApJ, 665, 369
Andersson B. G., Lazarian A., Vaillancourt J. E., 2015, ARA&A, 53, 501
Cantat-Gaudin T. et al., 2018, A&A, 618, A93
Capps R. W., Coyne G. V., Dyck H. M., 1973, ApJ, 184, 173
Carraro G., Vázquez R. A., Costa E., Ahumada J. A., Giorgi E. E., 2015, AJ, 149, 12
Cashman L. R., Clemens D. P., 2014, ApJ, 793, 126
Clayton G. C., Mathis J. S., 1988, ApJ, 327, 911
Coyne G. V., Kruszewski A., 1969, AJ, 74, 528
Davis L., Jr., Greenstein J. L., 1951, ApJ, 114, 206
Dolginov A. Z., Mitrofanov I. G., 1976, Ap&SS, 43, 291
Draine B. T., Weingartner J. C., 1996, ApJ, 470, 551
Efron B., 1979, Ann. Stat., 7, 1
Efron B., Tibshirani R., 1994, An Introduction to the Bootstrap. Chapman and Hall/{CRC}, New York
Eswaraiah C., Pandey A. K., Maheswar G., Medhi B. J., Pandey J. C., Ojha D. K., Chen W. P., 2011, MNRAS, 411, 1418
Eswaraiah C., Pandey A. K., Maheswar G., Chen W. P., Ojha D. K., Chandola H. C., 2012, MNRAS, 419, 2587
Fosalba P., Lazarian A., Prunet S., Tauber J. A., 2002, ApJ, 564, 762
Gaia Collaboration, 2016, A&A, 595, A1
Gaia Collaboration, 2018, A&A, 616, A1
Gerakines P. A., Whittet D. C. B., Lazarian A., 1995, ApJ, 455, L171
Goodman A. A., Jones T. J., Lada E. A., Myers P. C., 1992, ApJ, 399, 108
Goodman A. A., Jones T. J., Lada E. A., Myers P. C., 1995, ApJ, 448, 748
Haisch B. M., Cassinelli J. P., 1976, ApJ, 208, 253
Hall J. S., 1949, Science, 109, 166
Heiles C., 1996, ApJ, 462, 316
Heiles C., 2000, AJ, 119, 923
Hiltner W. A., 1949a, ApJ, 109, 471
Hiltner W. A., 1949b, Science, 109, 165
Hiltner W. A., 1956, ApJS, 2, 389
Hoang T., Lazarian A., 2016, ApJ, 831, 159
Hoang T., Lazarian A., Andersson B. G., 2015, MNRAS, 448, 1178
Hoang T., Tram L. N., Lee H., Diep P. N., Ngoc N. B., 2021, ApJ, 908, 218
Il'in V. B., Efimov Y. S., Khudyakova T. N., Prokopjeva M. S., Varivoda V. V., 2018, MNRAS, 475, 5535
Jones R. V., Spitzer Lyman J., 1967, ApJ, 147, 943
Jones T. J., Klebe D., Dickey J. M., 1992, ApJ, 389, 602
Jones T. J., Bagley M., Krejny M., Andersson B. G., Bastien P., 2015, AJ, 149, 31
Kharchenko N. V., Piskunov A. E., Röser S., Schilbach E., Scholz R. D., 2005, A&A, 438, 1163
Kharchenko N. V., Piskunov A. E., Schilbach E., Röser S., Scholz R.-D., 2013, A&A, 558, A53
Kim S.-H., Martin P. G., 1994, ApJ, 431, 783
Lazarian A., 2003, J. Quant. Spectrosc. Radiat. Transfer, 79, 881
Lazarian A., 2007, J. Quant. Spectrosc. Radiat. Transfer, 106, 225
Lazarian A., Hoang T., 2007, MNRAS, 378, 910
Lazarian A., Hoang T., 2021, ApJ, 908, 12
Lindegren L. et al., 2018, A&A, 616, A2
Mathis J. S., 1986, ApJ, 308, 281
Medan I., Andersson B. G., 2019, ApJ, 873, 87
Medhi B. J., Maheswar G., Pandey J. C., Kumar T. S., Sagar R., 2008, MNRAS, 388, 105
Medhi B. J., Maheswar G., Pandey J. C., Tamura M., Sagar R., 2010, MNRAS, 403, 1577
Moffat A. F. J., 1974, A&AS, 16, 33
Orsatti A. M., Vega E., Marraco H. G., 1998, AJ, 116, 266
Pandey A. K. et al., 2013, ApJ, 764, 172
Poeckert R., Marlborough J. M., 1978, ApJS, 38, 229
Purcell E. M., 1979, ApJ, 231, 404
Rautela B. S., Joshi G. C., Pandey J. C., 2004, Bull. Astron. Soc. India, 32, 159
Schmidt G. D., Elston R., Lupie O. L., 1992, AJ, 104, 1563
Scott D. W., 1979, Biometrika, 66, 605
Serkowski K., 1968, ApJ, 154, 115
Serkowski K., 1973, Greenberg J. M., van de Hulst H. C., eds, Proc. IAU Symp. Vol. 52, Interstellar Dust and Related Topics. Kluwer, Dordrecht, p. 145
Serkowski K., Mathewson D. S., Ford V. L., 1975, ApJ, 196, 261
Singh S., Pandey J. C., 2020, AJ, 160, 256
Singh S., Pandey J. C., Yadav R. K. S., Medhi B. J., 2020, AJ, 159, 99
Soam A. et al., 2021, AJ, 161, 149
Spitzer L., 1978, Physical processes in the interstellar medium. Wiley, New York, NY
Stephenson C. B., Sanduleak N., 1971, Publ. Warner & Swasey Obs., 1, 1
Vaillancourt J., Andersson B. G., Lazarian A., 2013, Proc. Sci., the Life Cycle of Dust in the Universe: Observations, Theory, and Laboratory Experiments. SISSA, Trieste, PoS#003
Vaillancourt J. E., Andersson B. G., Clemens D. P., Piirola V., Hoang T., Becklin E. E., Caputo M., 2020, ApJ, 905, 157
Vergne M. M., Feinstein C., Martínez R., 2007, A&A, 462, 621
Vergne M. M., Feinstein C., Martínez R., Orsatti A. M., Alvarez M. P., 2010, MNRAS, 403, 2041
Vergne M. M., Feinstein C., Martínez R. E., 2018, RMxAA, 54, 293
Voshchinnikov N. V., 2012, J. Quant. Spectrosc. Radiat. Transfer, 113, 2334
Voshchinnikov N. V., Das H. K., 2008, J. Quant. Spectrosc. Radiat. Transfer, 109, 1527
Voshchinnikov N. V., Henning T., Prokopjeva M. S., Das H. K., 2012, A&A, 541, A52
Voshchinnikov N. V., Il'in V. B., Das H. K., 2016, MNRAS, 462, 2343
Waldhausen S., Martínez R. E., Feinstein C., 1999, AJ, 117, 2882

Wang J.-W., Lai S.-P., Eswaraiah C., Clemens D. P., Chen W.-P., Pandey A. K., 2017, ApJ, 849, 157
Waskom M. et al., 2021a, mwaskom/seaborn: v0.11.2 (August 2021), Zenodo, available at https://doi.org/10.5281/zenodo.592845
Waskom M. L., 2021b, J. Open Source Softw., 6, 3021
Whittet D. C. B., 1992, News Lett. Astrono. Soc. New York, 4, 15
Whittet D. C. B., van Breda I. G., 1978, A&A, 66, 57
Whittet D. C. B., Martin P. G., Hough J. H., Rouse M. F., Bailey J. A., Axon D. J., 1992, ApJ, 386, 562
Whittet D. C. B., Gerakines P. A., Carkner A. L., Hough J. H., Martin P. G., Prusti T., Kilkenny D., 1994, MNRAS, 268, 1
Whittet D. C. B., Gerakines P. A., Hough J. H., Shenoy S. S., 2001, ApJ, 547, 872
Whittet D. C. B., Hough J. H., Lazarian A., Hoang T., 2008, ApJ, 674, 304
Wilking B. A., Lebofsky M. J., Rieke G. H., 1982, AJ, 87, 695

This paper has been typeset from a TEX/LATEX file prepared by the author.